Master's Thesis

Synthesis and Characterization of Resorcinol-Formaldehyde (RF) and Carbon Aerogel Microbeads by Dropping Method

Faculty of Mathematics and Natural Sciences
University of Cologne

M. Sc. Chemistry

Submitted by:

Thomas Anklam

Cologne, February 2021

First reviewer: Prof. Dr. Barbara Milow

Second reviewer: Prof. Dr. Mathias Wickleder

Danksagung

An dieser Stelle möchte ich mich herzlich bei dem DLR Köln-Porz und insbesondere bei Frau Prof. Dr. Barbara Milow für die Möglichkeit an diesem interessanten Thema zu arbeiten bedanken.

Vielen Dank Herr Prof. Dr. Wickleder für die Übernahme des Zweitprüfers.

Ein besonderes Dankeschön möchte ich auch an Herrn Dr. Seeni Meera Kamal Mohamed für die Betreuung dieser Arbeit und die zahlreichen spannenden wissenschaftlichen Diskussionen ausrichten.

Danke ebenfalls an das gesamte Aerogel-Team für die angenehme Arbeitsatmosphäre trotz Pandemie-Umständen, für die interessanten Diskussionen, für die Hilfsbereitschaft und natürlich auch für das Korrekturlesen und die hilfreichen Anmerkungen!

Vielen Dank an die Analytik Abteilung, insbesondere an Frau Rebekka Probst, Herrn Alexander Francke, Herrn Dr. Klemens Kelm und Herrn Frederic Kreps für die Aufnahme der SEM Bilder und XRD Diffraktogramme.

Zu guter Letzt bedanke ich mich bei meinen Eltern, Helena und Wilhelm Anklam, die mich nicht nur während dieser Arbeit, sondern auch während des gesamten Studiums unterstützten und es ermöglichten.

Eidesstattliche Erklärung

Hiermit versichere ich, Thomas Anklam, an Eides statt, dass ich die vorliegende Arbeit mit dem Thema

"Synthesis and Characterization of Resorcinol-Formaldehyde (RF) and Carbon Aerogel Microbeads by Dropping Method"

- selbstständig und ohne die Benutzung anderer als der angegebenen Hilfsmittel angefertigt habe.

  Alle Stellen, die wörtlich oder sinngemäß aus veröffentlichten oder nicht veröffentlichten Schriften entnommen wurden, sind als solche kenntlich gemacht.

  Die Arbeit ist in gleicher oder ähnlicher Form oder auszugsweise im Rahmen einer anderen Prüfung noch nicht vorgelegt worden.

  Ich versichere, dass die eingereichte elektronische Fassung der eingereichten Druckfassung vollständig entspricht.

Köln, 19.02.2021

(Ort, Datum)

Table of Contents

List of Abbreviations

ATR-IR	Attenuated total reflection-infrared
BET	Brunauer-Emmett-Teller
C	Catalyst
CB	Carbon aerogel microbeads
CBa	Carbon aerogel microbeads – pH adjusted precursor
conc.	Concentration
F	Formaldehyde
H	Hydrochloric acid
N	Nitric acid
R	Resorcinol
R/C	Resorcinol/catalyst ratio
RF	Resorcinol-formaldehyde
R/F	Resorcinol/formaldehyde ratio
RFB	Resorcinol-formaldehyde aerogel microbeads
RFBa	Resorcinol-formaldehyde aerogel microbeads – pH adjusted
R/W	Resorcinol/water ratio
SEM	Scanning electron microscopy
vol.	Volumetric
W	Water
WAXS	Wide angle X-ray scattering
w/o	Without
wt.	Weight

1. Origin of the Problem

Aerogels are typically produced in the shape of monoliths. However, various applications require aerogels in the shape of spherical beads or particles.[1]

Resorcinol-Formaldehyde (RF) aerogel beads with various sizes, size distributions and shapes can be produced by an inverse emulsification approach[2] or by grinding monoliths[3]. These processes have some disadvantages like problematic reproducibility and upscaling or the need of additional washing steps. Other efficient methods to produce microbeads have been reported for polysaccharide aerogels. These methods involve syringe-dropping and mechanical cutting with a JetCutter.[1a, 4] All of these methods are described in a later section. Especially, dropping is an interesting method for pioneering studies on the lab scale. It is quite challenging to shape RF sols as spherical beads in terms of dropping because of their low viscosity.[5] Hence, a thickening agent is required to control the viscosity and also the bead's properties, especially their size and shape.[1a, 6] Moreover, the thickening agent should not react with other chemicals in the sol. Typically, polysaccharide based thickening agents like Xanthan gum, Locust bean gum, Arabic gum and Guar gum are used in the food industry.[7] They are of special interest, since they are non-toxic and environmentally friendly.

One important application of RF- and carbon aerogel beads is the sand casting process. This process is used in the foundry industry to produce metals or alloys with a desired shape. In this process, the melt of a certain metal or alloy is poured into a mold made from sand and a binder, which binds the sand grains to give stability to the mold. Cavities in the product are produced by placing cores in the mold. Cores are also often made from sand and binder combinations. The mold and especially the core are often exposed to very high temperatures ranging from 750–1600 °C. These high temperatures cause decomposition of the binder, which leads to the formation of toxic gases and cracks, thus resulting in defects of the casting part like blow holes or to veining (Fig. 1). To avoid these problems, aerogels in the form of granules have been mixed with the sand prior to the application of the binder. The aerogel granules must have sizes in the region of the sand grains to achieve a homogenous miscibility.[8] Some sands typically used by the foundry industry have grain sizes ranging from 0.1–1.0 mm.[8b]

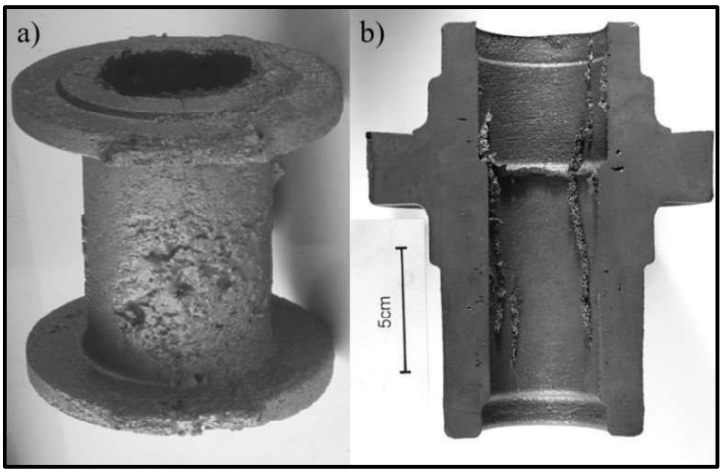

Figure 1: Common defects in the form of a) blow holes[9] and b) veining[10], occurred in casting parts made by a sand casting process.

The main aim of this masters' thesis is to produce RF aerogel beads with the addition of a thickening agent to the RF sol. A suitable dropping process will be found, and the products will be analyzed with sorption isotherms and morphological and spectroscopical methods. Furthermore, RF microbeads will be carbonized to form carbon microbeads, since they are especially interesting for the sand-casting process due to their high specific surface area and porosity.

2. State of the Art

Open porous nanostructured solids that are prepared by a sol-gel process with subsequent drying are generally referred to as 'aerogels'. They can consist of inorganic metal oxides, biopolymers, phenols, proteins, polyols, carbon allotropes or anything that can be gelled. Aerogels can further be classified according to their pore sizes as microporous (<2 nm), mesoporous (2–50 nm) and macroporous (>50 nm) or according to the drying process called as 'xerogels' (subcritically dried with large shrinkage), 'cryogels' (freeze-dried) and 'aerogels' (supercritically dried with minimal shrinkage). They possess remarkable properties like low densities (0.02–0.2 g/cm^3), low thermal conductivities (0.005–0.1 W/mK), low speed of sound (~100 m/s), high porosities (up to 99.9%) and high specific internal surface areas (100–3000 m^2/g), which make them especially interesting.[11]

2.1 RF Aerogels

More frequently used organic aerogels are prepared by a sol-gel reaction between resorcinol (R) and formaldehyde (F) and referred to as 'RF aerogels'. RF aerogels have porosities of about 90–98%, thermal conductivities as low as 0.012 W/mK, envelope

densities of 0.05–0.3 g/cm^3 and specific surface areas up to 1500 m^2/g. They are further not flammable and non-toxic.

The first step of the reaction is an electrophilic aromatic substitution (S_EAr) at R with F (Scheme 1).[11]

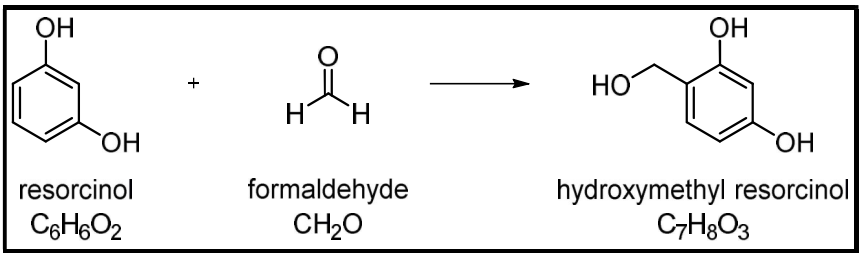

Scheme 1: Formation of hydroxymethyl resorcinol from S_EAr of R with F.[11]

The resulting hydroxymethyl resorcinol can react further in a S_EAr reaction to form multi-substituted resorcinol derivatives. This step is followed by a polycondensation reaction between the hydroxymethyl resorcinol molecules resulting in methylene and methylene ether groups (Scheme 2).[11]

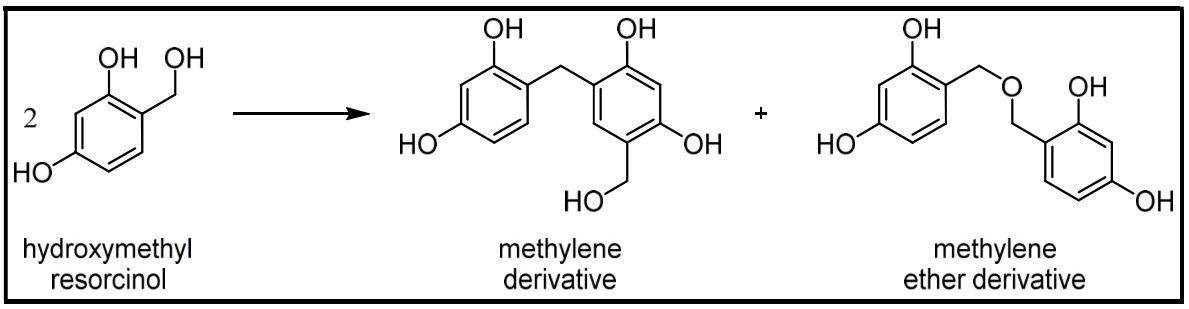

Scheme 2: Polycondensation between two hydroxymethyl resorcinol molecules forming either methylene or methylene ether groups.[11]

The structure and the properties of the resulting gel strongly depend on the following conditions: ratios of R/C, R/F and R/W, pH of the sol, catalyst type, gelation temperature, aging time and drying method.[11] Al-Muhtaseb et al.[12] had published an extensive review concerning the synthesis parameters of RF aerogels. The value of R/F ratio <1 is necessary to obtain the desired network structure, which is referred to as the *'Resol'* structure. An increase in the R/W ratio results in an increased density and reduced porosity. The R/C value or pH of the sol has a large influence on the aerogels structure and properties. A precursor sol without catalyst has a pH between 3 and 4. The gelation process takes the longest time at this pH-value (Fig. 2). Both acidic and basic conditions result in a decreased gelation time.

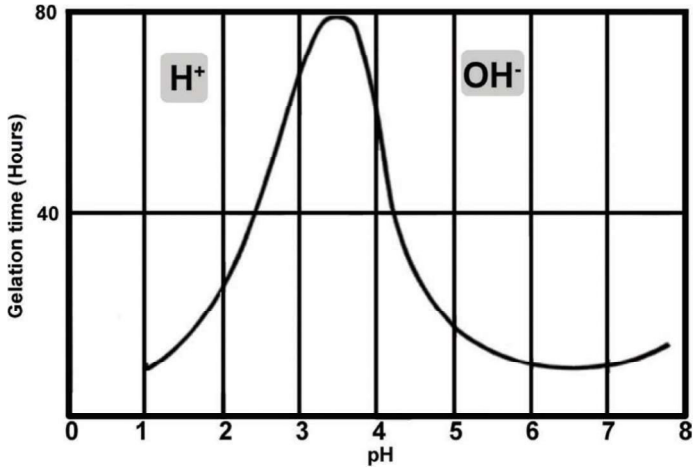

Figure 2: RF gelation time in dependence of the pH value.[12]

The mechanism is different for both conditions and leads to aerogel products with different properties.

In a typical reaction process for base catalysis, R and F are dissolved in deionized water (W) and stirred before Na_2CO_3 is added as catalyst (C). After the stirring, the mixture is typically transferred to a sealed container and stored in an oven at temperatures between 40–80 °C for up to 7 days to perform gelation and aging.[11] In basic conditions, the S_EAr reaction is faster than the polycondensation reaction. R is activated by deprotonation at the phenolic oxygen and reacts fast with F to form multi substituted hydroxymethyl resorcinol molecules (Scheme 1). These molecules react with each other resulting in polycondensation (Scheme 2) to form clusters, the size of which is determined by the pH value. The higher the pH, the more anions are formed initially which then react at the same time to form more but smaller clusters. Smaller clusters result in small pores after networking with other clusters (Fig. 3a). The surface area is therefore increased, whilst the stability against ambient drying conditions is decreased. Typically, Na_2CO_3 is used as a basic catalyst, resulting in a pH of 6.5–7.4. The polycondensation reaction is hindered for a pH >9.0.

In acidic conditions, the polycondensation reaction is faster than the S_EAr reaction. F molecules are activated by protons and react in a S_EAr reaction with R to form hydroxymethyl resorcinol molecules. These molecules are protonated at the aliphatic alcohol groups and water leaves the molecule, which makes it a good electrophile for another S_EAr reaction with R. Therefore, lots of methylene bridges are formed under acidic conditions. Primary particles are big (Fig. 3b), since the polycondensation reaction is much faster than the S_EAr reaction. RF aerogels produced under acidic conditions therefore have big pore volumes, small surface areas

and enhanced stability against ambient drying conditions. The reactants precipitate if the pH is lower than 0.8.

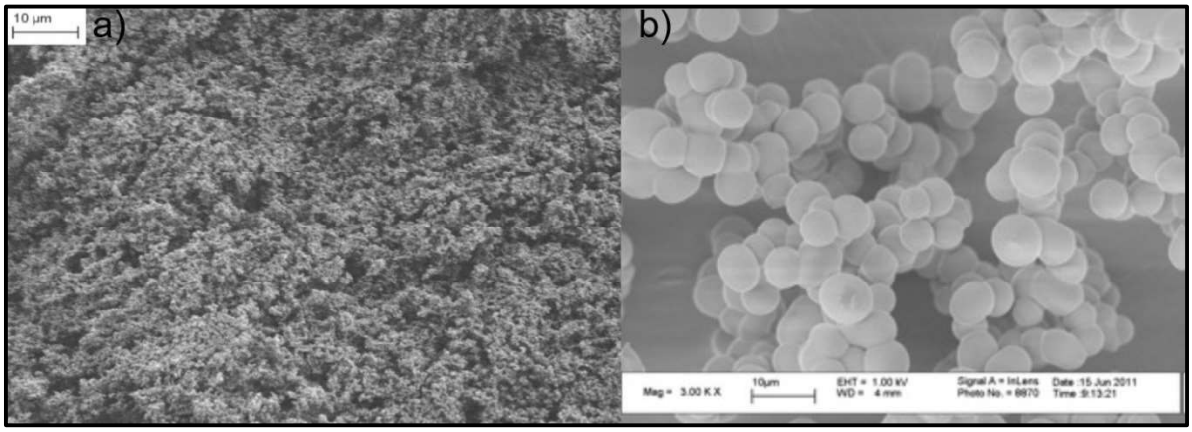

Figure 3: SEM images of RF aerogels synthesized under a) basic[13] and b) acidic[14] conditions.

The synthesis can also be performed in a consecutive order of basic and acidic conditions. Laskowski et al. have pre-gelled RF sol under basic conditions and added citric acid after various pre-gelation times (Fig. 4).[15]

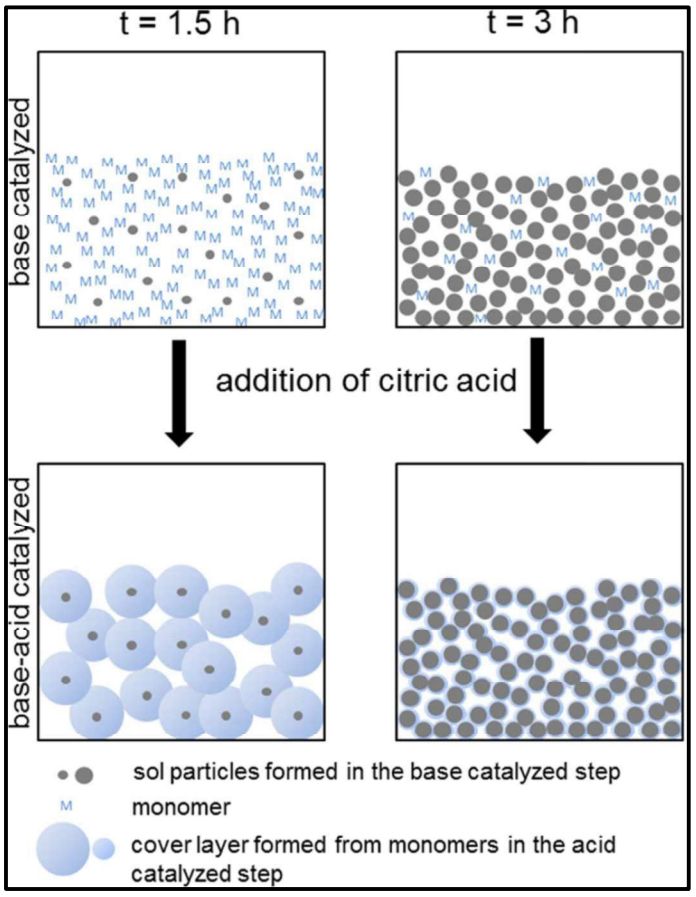

Figure 4: Scheme of base-acid catalyzed synthesis of RF aerogels. If the acid is added after a shorter pre-gelation time under basic conditions the gel will contain fewer but bigger particles, while it will contain more but smaller particles after a longer pre-gelation time.[15]

Depending on the pre-gelation time before acid addition, different microstructures and properties of the gels were obtained. In the first step under basic conditions, resorcinol anions are formed and the longer the pre-gelation time under basic conditions, the more small particles are formed (Fig. 4, base catalyzed step). In the second step under acidic conditions, particle growth and cluster formation occur. Therefore, if the acid is added earlier, the gel will contain of fewer but bigger particles, while the sol contains of more but smaller particles if the acid is added at a later point (Fig. 4, acid catalyzed step). In consequence of the varying microstructure other properties like the surface area will also be different.[15]

The water in aged gels is often exchanged with other organic solvents like acetone and alcohols (e.g. methanol, ethanol). In some cases, heat is applied to increase diffusion of the solvents into the pores of the gel. These solvents have lower surface tensions and boiling points than water, which is beneficial for subcritical and ambient drying. Further, they are also miscible with supercritical CO_2, which is necessary for supercritical CO_2 drying. In some cases, trifluoro acetic acid is used before the first solvent exchange step to enhance the crosslinking of clusters. Ambient drying is time consuming and requires stable gels to prevent excessive shrinkage. Therefore, the gels should have large pore sizes and high solid concentrations.[16] Subcritical drying is performed at elevated temperatures and reduced pressure for a few days and results in RF xerogels with shrinkage up to 68%. Supercritical drying with CO_2 is one of the best methods to obtain high quality aerogels with a very low shrinkage, but it requires a time-consuming solvent exchange. Freeze drying is an economical and easy method to dry RF gels but has the disadvantage of the formation of big pores due to ice crystal formation in the gel. As an alternative method, microwave drying has been reported as a good drying method for gels with big pore sizes or gels that were prepared under ultrasonic irradiation.[17]

Furthermore, RF aerogels are especially interesting because they can be transformed to carbon aerogels.

2.2 Carbon Aerogels

Carbon aerogels (Fig. 5b) can be produced by carbonization of various organic aerogels (e.g. RF[12] (Fig. 5a), phenol furfural[18], polyisocyanate[19], polyvinyl chloride[20]) and biopolymeric aerogels (e.g. starch[21], pectine[22], alginic acid[23]).

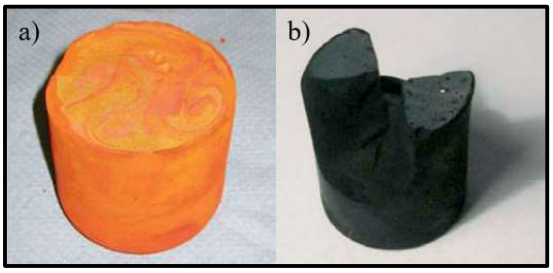

Figure 5: Photographs of a) RF aerogel and b) carbon aerogel monoliths.[24]

Carbonization of RF aerogel is typically carried out under inert conditions (Ar, N_2) at temperatures ranging between 600–2100 °C.[25] Temperatures <1000 °C lead to pyrolysis while temperatures >1000 °C lead to graphitization of the material.[26]

They can furthermore be doped with other heteroatoms[27]/metals[28] or activated by introduction of functional groups with O_2 (plasma), HNO_3 or H_3PO_4 or by etching with CO_2, NaOH or KOH.[12]

Carbon samples prepared from RF aerogels typically exhibit a shrinkage of 20–30% and a mass loss of approx. 50%. They generally have a similar microstructure to their precursor aerogels (spherical particles for RF precursors and fibrous structure for polysaccharide precursors) but can be altered by choosing the carbonization temperature. The surface area of carbon aerogels is increased significantly compared to RF aerogels due to the formation of micropores during the pyrolysis and the resulting loss of organic groups.[29] The micropore volume therefore increases and the mesopore volume decreases during the pyrolysis step. Specific surface areas as high as 4570 m^2/g and pore volumes as high as 4.9 cm^3/g have been reported.[30]

Carbon aerogels derived from RF aerogels have applications as electrode materials, catalyst carriers, and adsorbent materials for large molecules and heavy metals.[12, 29] Another interesting application is the use of carbon aerogels as additives for sand mixtures in the sand casting process.[8a]

2.3 RF- and Carbon Aerogels for Foundry Applications

B. Milow and *L. Ratke*[8a, 24] have given an extensive overview on the topic of aerogels for foundry applications in the form of a book chapter and journal articles, which are cited in the following section. Metals and alloys are often shaped by pouring their melts into molds that are a negative of the desired shape. Cavities in the product are produced by placing removable cores in the molds (Fig. 6). These molds can be reused or destroyed after each process. The latter is the case in the sand casting process, where the molds and cores are made up from various combinations of sands like quartz-, chromite-, zirconia or olivine sand and binders like clay, water glass, cement, plaster, organic resins, oils and carbohydrate binders.[8a]

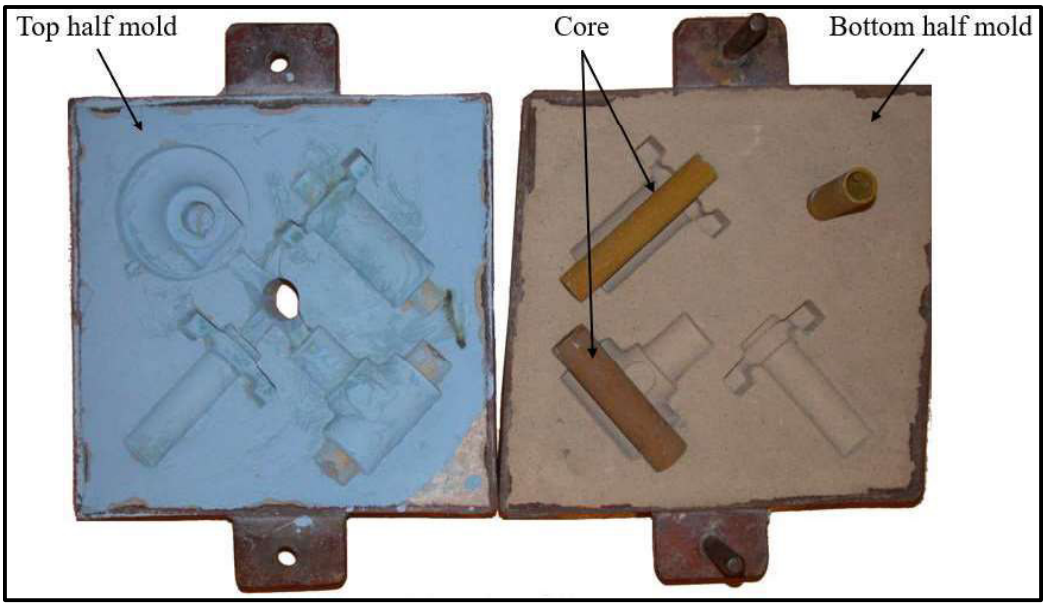

Figure 6: Images of molds and cores used in sand casting process.[31]

The combination of sand and binder must fit the temperatures of the casting. Light metal castings (Al, Mg) require temperatures of ~750 °C, non-ferrous heavy metal castings (Cu, brass, bronze, Ti) require temperatures of 900–1200 °C, cast iron requires 1350 °C and steel requires ~1600 °C.

There are some important requirements that sand/binder combinations must fulfill to be proper candidates for the sand-casting process. The mixture must not lump and have a good flowability to tickle easily in the molds. They should also have a big enough green strength and dry strength to be stable while handled in the process. They should have a good refractoriness to withstand the strain while the hot metal is poured and resist fluid friction to prevent sand grains getting into the melt. A good

deformability is also necessary to withstand the shrinkage stresses and prevent crumbling. Another important property is the gas permeability. Gases that are dissolved in the melt or decomposition products of the sand/binder mixture must be able to pass through the mold to prevent the blow hole formation in the casting part. Additionally, they must be resistant to metal penetration to prevent veining. They must have a fine structure, so that a fine surface of the casting is guaranteed. Cores must have a good collapsibility to be easily removed from the casting part after the process. These properties can be to some degrees tuned by optimizing the sand type, grain size and size distribution, binder type, binder amount and curing temperature, but the formation of defects remains a problem.

Aerogels are used as binder material or as particular additive (Fig. 7) and have some properties that are especially beneficial for foundry applications.

Figure 7: Sand casting cores made with 1.5% aerogel additive. Brown: RF aerogel, buff colored: silica aerogel and black: carbon aerogel.[24]

In a typical process, 0.5–10% of the sand is substituted by the aerogel beads and then mixed with a binder before core shooting and hardening. The size of the aerogel beads should be in the region of the sand grains to guarantee a good miscibility.[8a, 24] The high surface area of aerogels results in an enhanced physisorption of decomposition gases from binders and thus reduces the formation of defects like blowholes. Further, depending on the type of aerogel used, the gases can react with the aerogel, resulting in chemisorption.

The thermal conductivities of cores decreased (by 8–20%) upon aerogel bead addition (1.0–2.5 vol%).[24] The cooling time of the melt is delayed by 10–20% due to the reduced thermal conductivity. Lower casting temperatures and thin-walled casting

are therefore possible. Nevertheless, depending on the binder, enhanced binder decomposition can occur due to the longer impact of the heat. The use of aerogels as additives further leads to the advantage of compensating the expansion of quartz sand upon heating, due to their elastic properties.

The addition of aerogel beads to a sand (F34) and binder (resin) combination resulted in an enhanced gas permeability.[24] Moreover, the surface roughness of brass and aluminum castings has been remarkably improved by the addition of various aerogel beads (Fig. 8).[24]

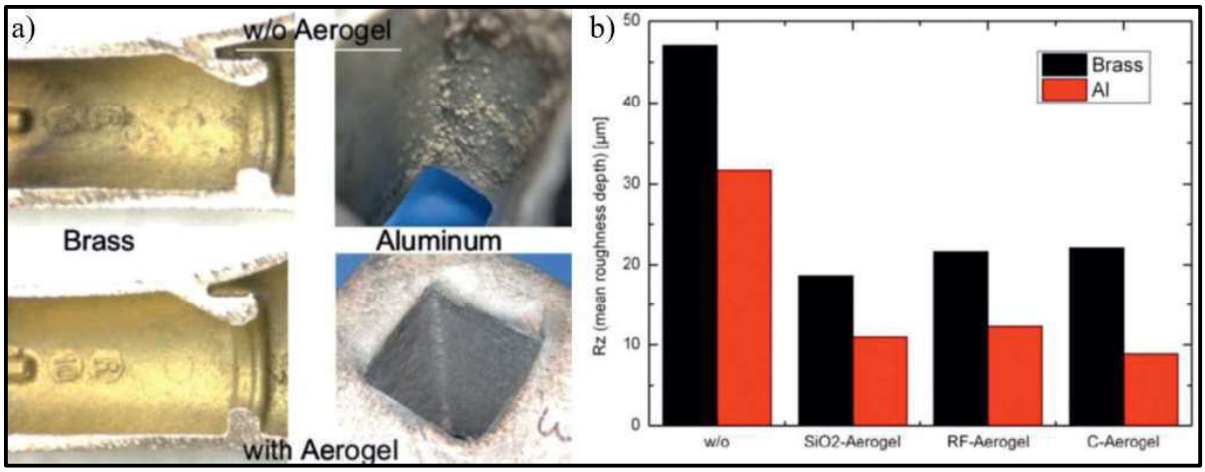

Figure 8: a) Comparison of the surface roughness of brass and aluminum castings produced using cores with and without aerogel additives. b) Mean roughness depth of brass and aluminum casting produced with various aerogel additives and without aerogel additives.[24]

L. Ratke et al.[8b] have patented a process, in which a water-soluble core, made from quartz and corundum sands mixed with silica aerogel particles and bound by water glass, is used in a light metal sand-casting process. The core can be easily removed by water with temperatures from 30–100 °C in a time frame ranging from few seconds to few minutes after the cooling of the casting. Other hydrophilic aerogels like RF aerogels can also be used. A remaining challenge in this field is the cost effective mass production of aerogel beads.[8a]

2.4 Microbeads of RF- and Carbon Aerogels

Various methods can be used to produce microbeads of aerogels. Very recently, Schwan et al.[3] have produced particles by grinding stiff, ductile and flexible carbon aerogel monoliths (Fig. 9) with sanding paper (lowest energy input) or by milling them with a cryo-shaker mill (low energy input) and a ball mill (high energy input).

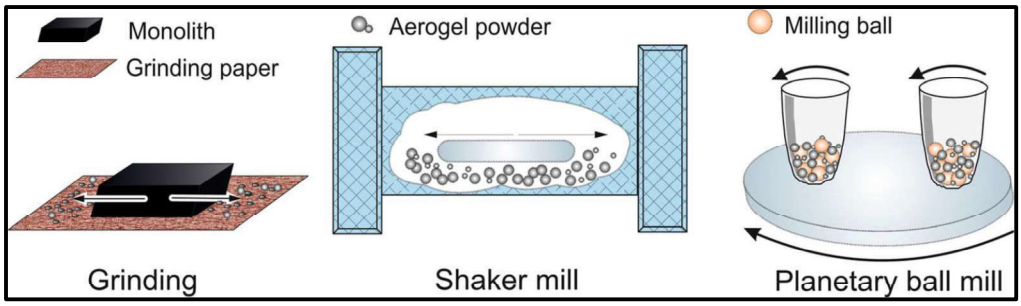

Figure 9: Various pulverization techniques with different energy inputs.[3]

Particles generated by these methods have sizes ranging between 1–40 µm. It was shown that especially flexible aerogels underwent significant microstructure changes. Microstructure changes of ductile and stiff aerogels were rather minor. Grinding with sanding paper appeared to be not reproducible, since the pressure used to grind varies from operator to operator. Pulverization of carbon aerogels by grinding them in a mortar is also reported in literature.[32]

A more common method to produce aerogel beads that is often used for RF aerogel beads is the inverse emulsion approach. Generally, a solution of aqueous RF sol is added to an immiscible liquid that contains an emulsifier and stirred thoroughly. The gelation can be triggered chemically or physically. The hydrogel beads can be filtered, washed and dried to obtain aerogel beads (Fig. 10).[1a]

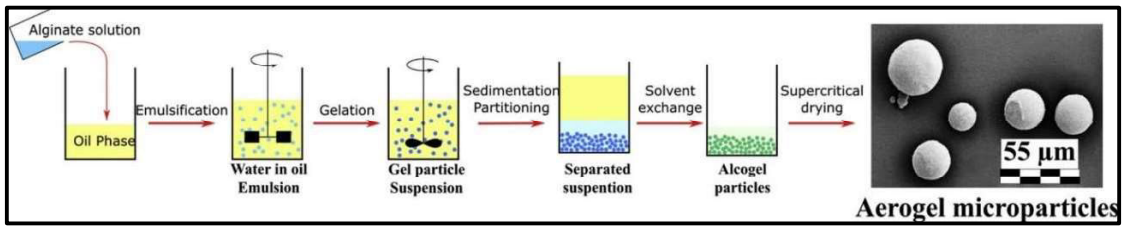

Figure 10: Scheme of the inverse emulsion approach, with alginate aerogels.[2f]

Apart from RF aerogels[2a-e], other microbeads produced by inverse emulsion approach include silica aerogel[33], polyurea aerogel[34], polyimide and polybenzoxazine aerogels[35], alginate aerogel[2f, 36], carrageenan aerogel[37] and pectin aerogel[38]. Carbon microspheres are typically produced by the carbonization of

carbon containing aerogel microspheres.[2a-e, 35]

The continuous phase/emulsifier can consist of PEG-9 lauryl alcohol or cetyltrimethyl-ammonium bromide in hexane[34], mineral oil[2b], sorbitan monooleate in cyclohexane[2a-c, 2e], peanut oil[2d], sorbitan monooleate in paraffin oil[2f], sorbitan trioleate and hypermer™ 1599 in cyclohexane[35] and canola oil[38].

RF aerogel microbeads produced by this method typically have sizes in the region of 10–1000 µm.[2a, 2c, 2d, 34] Even bigger beads with sizes up to 3 mm were reported in a patent.[2b] The size of the beads can be increased by decreasing the stirring speed during the gelation and also by increasing the viscosity of the sol.[2c] The size of the beads depends further on the collision rate of the droplets, which can be tuned by the water/oil ratio (typically 1:2–1:10).[1a] Further, the reaction rate, which can be tuned by the chemical composition of the sol, has an impact on the bead size.[2b] The amount of emulsifier and its hydrophilic-lipophilic balance (HLB) value are also important. The HLB value, describes the ratio of hydrophilic and lipophilic parts of a emulsifier and should be in the region of 3–6.[1a]

An approach to scale up the inverse emulsion method for aerogel microbead production is reported in literature.[2f] The major drawback of this method is, that the beads are polydisperse in nature and need to be washed from the lipophilic medium.[1a]

The syringe dropping method, which is frequently used for polysaccharide aerogel microbeads, would be an elegant method for the production of RF aerogel microbeads on a laboratory scale.[1a, 6] The dropping is based on gravitational forces and can be further supported by vibrations or electrostatic forces (Fig. 11).

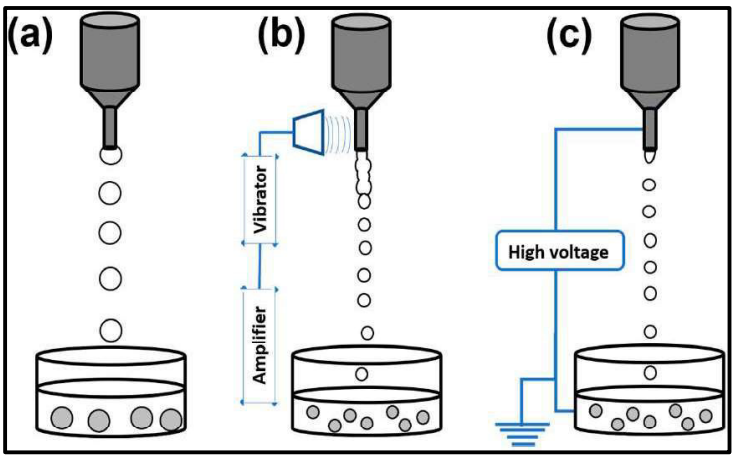

Figure 11: Illustration of dropping methods. (a) gravitational dropping, (b) vibration assisted dropping and (c) electrostatic force assisted dropping.[1a]

To the best of my knowledge, no published reports were available on the production of spherical RF aerogel microbeads by conventional dropping methods. The dropping method involves the dropping of a sol into a gelation bath. Typically syringes or pipettes are used to produce droplets.[1a]

With a conventional dropping method (Fig. 11a), beads with sizes of few millimeters are produced. The shape and size of the droplets are influenced by the surface tension, density and dynamic viscosity of the sol and the geometry of the nozzle and its distance from the gelation bath. The production capacity of this method is very low and viscosities of sols are usually limited to <200 mPa.s.[39] The vibration assisted dropping method (Fig. 11b) involves the destabilization of a liquid jet with superimposed vibrations. The sol is pressurized through a nozzle to produce a jet. The droplet size is typically twice the diameter of the nozzle and can be additionally controlled by the flow rate of the liquid. The major drawback of this method is that it is also usually limited to low viscosity sols (few hundred mPa.s). The electrostatic force assisted dropping method (Fig. 11c) involves the extrusion of a low viscosity sol through a charged nozzle. The electric field in addition to the gravitation pulls the liquid as droplets away from the outlet of the nozzle. An induced surface charge of the droplets prevents coalescence of the beads while falling. The disintegration of the droplets and their size depends on the viscosity of the sol, the nozzle diameter, the distance between the nozzle and the gelation bath and the applied voltage. Beads produced with this method are nearly monodispersed and can be as small as few tens of micrometers. Dropping methods have the advantages of being very simple and generally do not require any additives. The disadvantage though is the very low productivity and the limitation to low viscous sols.[1a] Aerogel beads of polyurea[40], agar[41], alginate[41], cellulose[42], chitin[41], chitosan[41], K-carrageenan[41], pectin[43] and starch[44] produced by dropping methods were reported in the literature.

The upscaling of aerogel microbead production can be carried out by mechanical cutting with a JetCutter (Fig. 12a). This method involves the cutting of a continuous liquid jet into cylinders with a rotating cutting disc. The cutting disc contains radially oriented wires. The cylinders fall into a gelation bath that is placed along their trajectory. Upon falling, they turn into spherical beads due to their surface tension. A small amount of the jet is lost during each cutting step (Fig. 12b).[1a]

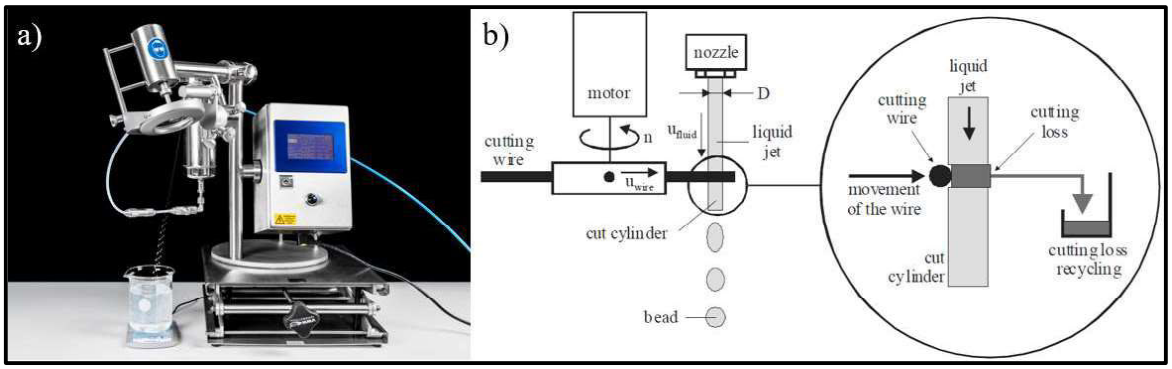

Figure 12: a) JetCutter from geniaLab GmbH at DLR[45] and b) illustration of the mechanical cutting method of a liquid jet with a JetCutter.[39]

Since the jet and the cutting disc have similar velocities, a perpendicular arrangement (Fig. 13a) of them results in distorted cylinders, which leads to additional spraying losses. This problem is reduced by using an inclination between the jet and the cutting disc (Fig. 13b).[39]

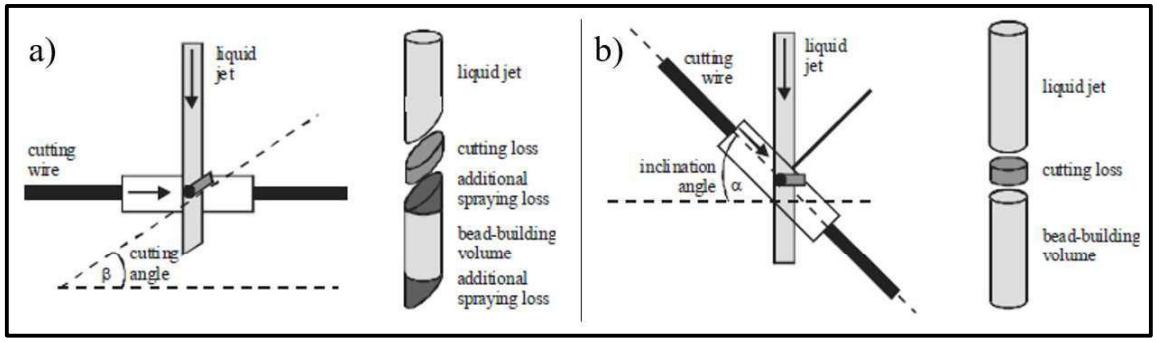

Figure 13: Detailed scheme of the cutting process for a) perpendicular arrangement and b) inclined arrangement of the jet and the cutter.[39]

The bead size can be tuned between few hundred micrometers and few millimeters by changing the nozzle diameters, jet velocities and cutting frequencies. Further, the gelation bath should be big enough for the amount of beads produced.[6] The advantages of the JetCutter method are very high productivity (several kg/h), the absence of additives, commercial availability and monodispersed beads. The disadvantages of this method are that small beads (<200 µm) can't be produced, the losses during cutting and the limited rheological properties of the solutions that are suitable. For sols with low viscosities (200–300 mPa.s), the loss from cutting increases with decreasing viscosities.[1a] Fluids that have successfully been turned into beads with a JetCutter include solutions of alginate, pectinate, chitosan, gelatin, cellulose and its derivatives, waxes, polymer melts and inorganic sols.[39]

The dropping and jet cutting methods have in common, that a proper gelation bath must be used. A proper gelation bath should induce the gelation whilst keeping

the shape of the droplet and preventing the droplets from agglomeration or coalescence. The gelation of polysaccharides is based on the precipitation of dissolved polymers and is induced by temperature, crosslinking agents such as ions or the pH value.[1a] Synthetic organic polymer aerogels on the other hand depend on the formation of the polymer itself from monomers in the gelation step. Therefore, the polymerization reaction should be triggered fast in the gelation bath.

In RF aerogel synthesis under common basic conditions, the gelation takes few hours up to few days for monoliths, as stated in a previous section. In case of acid-base catalyzed synthesis of RF monoliths, the gelation can be ranging from 1–5 min after adding 1.0 M acetic acid to the RF sol that has been aged for 2 h at 50 °C.[46] Moreover, as cited in a previous section, Laskowski et al. have induced the rapid gelation (2–5 min) of RF sol pre-gelled for 2 h under basic conditions by addition of citric acid (Fig. 14). If the pre-gelation time was not long enough (<1 h), a bakelite like structure formed instead of an aerogel.[15]

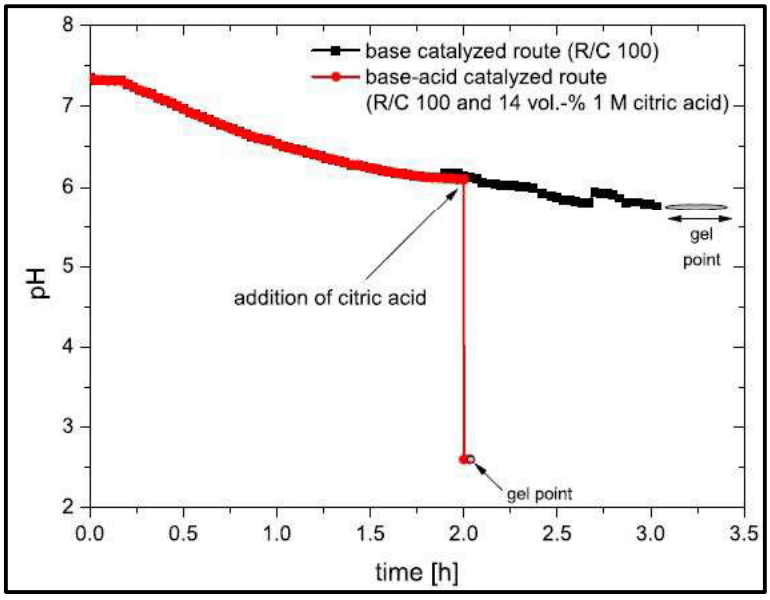

Figure 14: Graph of the pH dependent gelation time of a RF sol. The sol was pre-gelled under basic conditions at a pH-value ranging between 7–6 before citric acid was added to lower the pH value to 2.5 and thus induce instant gelation of the sol.[15]

The approach of choosing a gelation bath that increases the gelation rate chemically with an acid instead of physically stabilizing the droplets seems the best for RF chemistry when the previously discussed works are considered.[15, 46] Pre-gelation under basic conditions is expected to be necessary since it improves the microstructure of the resulting beads and allows a faster gelation afterwards and thus prevents dilution of the droplet upon dropping into the gelation bath. However, the major concern about

acidic conditions is that it influences the microstructure of the resulting beads. To prevent that only the acid determines the microstructure of the resulting aerogel, the sol should be pre-gelled as long as possible under basic conditions. The gelation bath medium should not be too viscous since it could result in destruction of the droplets upon the impact.

2.5 Thickening Agents for Aqueous Solutions

Controlling the dynamic viscosity of the precursor solution is of great interest since the size and shape of the beads generated by the syringe dropping method depends on its viscosity.[39] An increase in viscosity is referred to as thickening. The dynamic viscosity (μ) is the ratio between the shear stress (τ) and the shear rate ($\dot{\gamma}$) (eq. 1)[47] and can be described as the resistance of a fluid against shear flow.[48] A liquid with a higher viscosity will flow slower at a constant force.

$$\mu = \frac{\tau}{\dot{\gamma}} \tag{1}$$

Nevertheless, this equation is only true for *Newtonian* fluids (2 in Fig. 15). The dynamic viscosity itself can depend on the shear rate. For shear thickening (dilatant, 1 in Fig. 15) fluids the dynamic viscosity increases with increasing shear rate and for shear thinning (pseudoplastic, 3 in Fig. 15) fluids the dynamic viscosity decreases with increasing shear rate. Other special cases like *Bingham*-plastic fluid (4 in Fig. 15) and *Casson*-plastic fluids (5 in Fig. 15) are known. Here, a threshold shear stress is needed before the liquid flows in a newtonian or pseudoplastic way.[49]

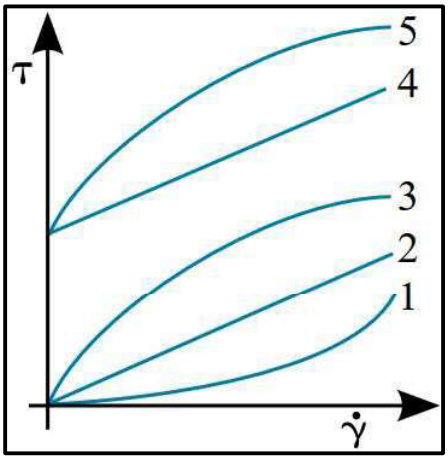

Figure 15: Shear stress-shear rate diagrams of various materials: 1) Shear thickening (dilatant) fluids, 2) *Newtonian* fluids, 3) Shear thinning (pseudoplastic) fluids, 4) *Bingham*-plastic fluids, 5) *Casson* fluids.[50]

The viscosity can depend on the temperature, the shear time, the concentration of the dispersed phase, the particles sizes, shapes and interactions between each other.[49] The viscosity of a liquid can be increased in various ways. For example, for most materials it can simply be cooled down.

Another way to increase the viscosity is to react the components of a material like in polymerization reactions. A common used method to increase the viscosity without changing other properties of the material is to add thickening agents. Thickening agents can be inorganic ones like clays and silica or organic ones like typically polysaccharides, proteins or other synthetic polymers like polyethylene glycols, polyvinyl alcohol, polyacrylates and polyurethanes.[51] They find application in the food-[7b], cosmetic-[52], pharmaceutical-[53], paint-[51], explosive-[54] and petrochemical industries[55]. For the current thesis, the thickening of aqueous RF sol solutions with an environmental-, health- and cost friendly agents is of special interest. Therefore, thickening agents used in the food-, cosmetic- and pharmaceutical industries are going to be considered. These are primarily biological polysaccharides.

In the following section, the rheological properties of commercially available thickening agents are going to be briefly reviewed concerning their application as thickeners for RF sols which could be used for microbead production by syringe dropping method.

Xanthan gum is probably the most common representative of polysaccharide thickening agents. It is composed of a 1,4-linked *β*-D-glucose backbone with a side chain composed of *β*- D-mannose- 1,4-*β*- D-glucosyl acid- 1,2-*α*-D-mannose. The internal mannose unit is O-acetylated, and about the half of the external mannose unit forms an acetal with pyruvic acid (Fig. 16). It is produced by the *Xanthomonas campestris* bacterium.[56]

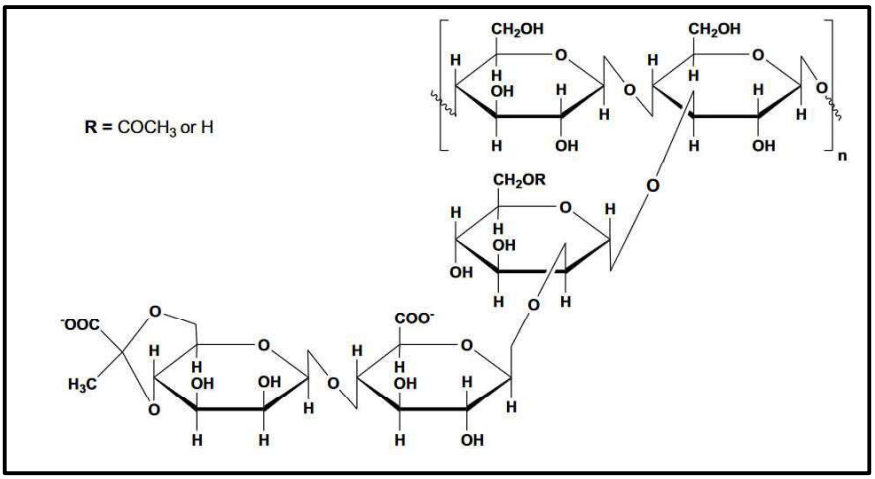

Figure 16: Chemical structure of Xanthan gum.[57]

Xanthan gum is dispersible in hot and cold water.[58] Aqueous Xanthan gum dispersions show shear thinning behavior and the viscosity is proportional to the concentration of Xanthan gum (Fig. 17).[59] Compared to other thickening agents, only a small amount is needed to increase the viscosity.[60]

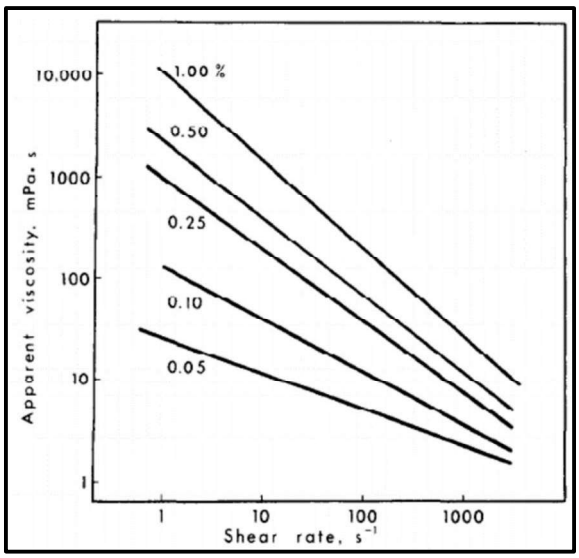

Figure 17: Frequency sweep of the viscosity of aqueous XG solutions with concentrations ranging from 0.05-1.00%.[59]

Lower concentrated dispersions have a stable viscosity in the region of pH 1–13. In the case of 1% dispersion, only minor viscosity changes from pH 3–12 are observed, while a lower pH value will decrease- and a higher pH value will increase the viscosity.[56a, 60-61] Further, the viscosity of Xanthan gum dispersion is temperature dependent and decreases strongly for increasing temperatures at lower shear rates. The viscosity is rather insensitive to temperature changes for low concentrations (0.1 and 0.2 wt.%).[62]

Welan gum is a material produced by *Alcaligenes* bacteria. The chemical structure is shown in Figure 18.[63]

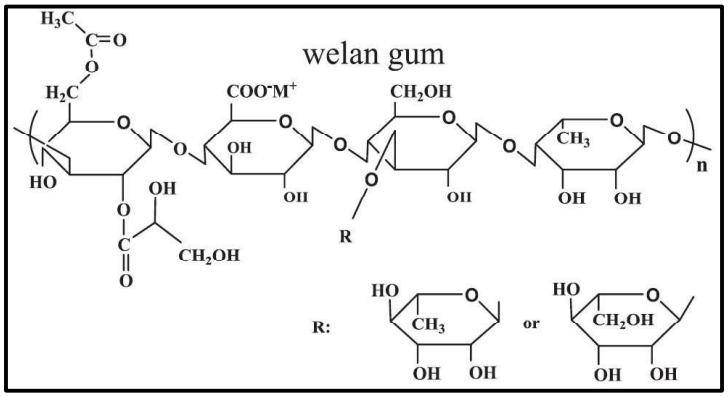

Figure 18: Structure of welan gum.[63]

Welan gum dispersions can be prepared at room temperature. They show shear thinning behavior and the viscosity is proportional to the concentration. Only a low amount of welan gum is needed to increase the viscosity. Moreover, Welan gum dispersions keep more of their viscosity when the temperature is increased compared to xanthan gum.[63]

Guar-, Tara- and Locust bean- gum have in common, that their major ingredients are galactomannans with similar structures. The chemical structure is shown in Figure 19.[64] The dispersibility in cold water correlates with the mannose/galactose ratio and is best for Guar gum and worst for Locust bean gum.[64-65]

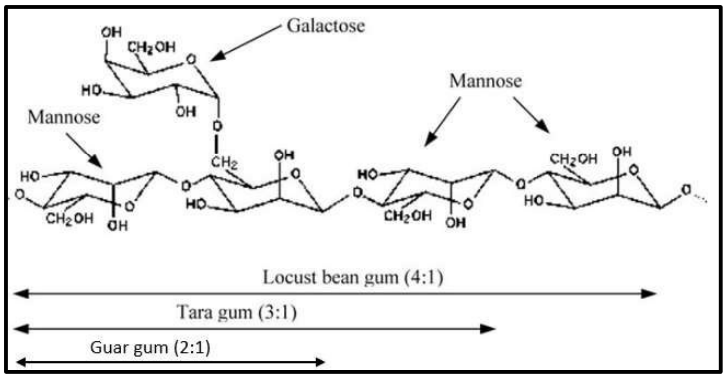

Figure 19: Comparison between the structures of Guar gum, Tara gum and Locust bean gum.[66]

Aqueous Guar gum dispersions show typical shear thinning behavior and the viscosity is proportional to the concentration.[65] Increasing temperatures result in a decreasing viscosity.[67] Further the viscosity is higher at acidic conditions, followed by neutral conditions and the lowest viscosity at basic conditions.[68] Tara gum dispersions show

a shear thinning behavior and the viscosity is proportional to the concentration. The dispersions generally show a stable viscosity for pH values ranging from 3–11, even though minor changes occur. They further show a decrease in viscosity for increasing temperatures. This effect was stronger for dispersions with lower concentrations.[64] Locust bean gum dispersions must be stirred at >80 °C in order to be dispersed. Aqueous dispersions show shear thinning behavior and the viscosity is proportional to the concentration.[65] The viscosity further strongly depends on the temperature. The temperature effect is stronger for dispersions that experience low shear rates. For a pH value ranging from 3–6, an influence on the viscosity is observed only for dispersions that experience low shear rates.[69]

Alginates are produced by various *Laminaria* brown algae. They are salts of alginic acid. The chemical structure is shown in Figure 20.

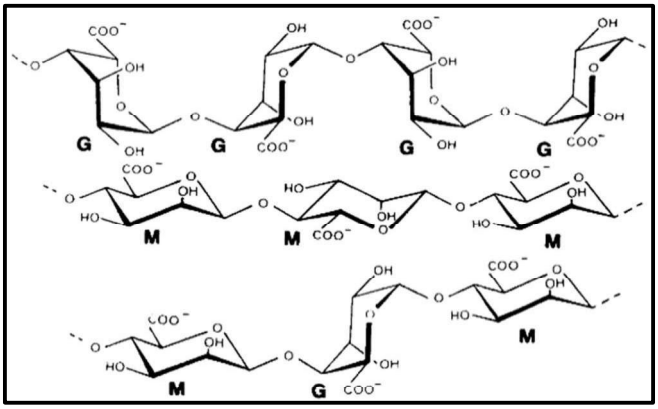

Figure 20: Chemical structure of alginate polysaccharide.[70]

Common water dispersible salts are e.g. Na-alginate, K-alginate or NH_4-alginate. Alginates gel by interaction with calcium ions. Too many monovalent cations like Na^+ and Cl^- result in solubility issues of alginates. Alginate dispersions typically exhibit shear thinning behavior.[70] The viscosity is increased with the molecular weights of the alginate polymers and the concentrations of the resulting dispersions. Further, the viscosity of alginate dispersions decreases with decreasing temperature at a rate of about 2.5%/°C. Alginate dispersions are stable for a pH range from 5–11. If the pH is <5, the viscosity starts to increase and if the pH is as low as 3–4, a gel will start to form.[71]

2.6 Preliminary Experiments

In preliminary unpublished experiments[5b], it was observed that a sol without thickening agent and reactant ratios of R/F = 0.74, R/W = 0.044 and R/C = 1500 could be dropped into 2 M formic acid after pre-gelation for 4.25 h at 60 °C to obtain jellyfish-like structures. The addition of a thickening agent gives control over the viscosity, reduces the gelation time, and is expected to lead to better results in terms of the gelation of the sol and the beads size and shape. First experiments with Na-alginate as thickening additive have been performed with concentrations of 1–3%.[72] The sol was pre-gelled for 1–1.5 h under basic conditions and dropped into 2M formic acid and 2M HCl. Since xanthan gum is a frequently used thickening agent with various applications, preliminary experiments have been performed with a sol that contained 0.1% and was dropped into 2M HCl, which led to stable spherical RF aerogel beads.[73]

3. Experimental Section

3.1 Materials

Resorcinol and Na_2CO_3 were purchased from SIGMA ALDRICH, Germany. Formaldehyde (23.5%) was purchased from CARL ROTH, Germany. Xanthan gum (XG) was obtained from DEUTERON GmbH, Germany (VT 930) as a gift sample. HCl solution (37%) and HNO_3 solution (2M) were purchased from PANREAC APPLICHEM ITW Reagents, Germany. Deionized water was used throughout the experiments.

3.2 Methods

Gelation, aging and drying of RF Beads was performed in a MEMMERT Universal Oven UF110 or a MEMMERT Universal Oven UF30 at 60 °C. The pH values were measured with a SevenEasy pH-meter from METTLER TOLEDO. The carbonization yields were calculated as percentual mass ratio before and after carbonization.

Average bead sizes were measured with a digital sliding caliper. 100 beads were measured for each sample.

The tapped density of beads was measured by weighing 2 ml of beads in a measuring flask after forming a close packing by tapping. The skeletal density of beads was measured using an AccuPyc II 1340 Helium Pycnometer from MICROMERITICS. The purge- and cycle fill pressure was set to 19.500 psig and equilibration was ended at a rate of 0.0050 psig/min. The samples were purged 10 times for RF Beads and 30 times for carbon beads and measured 10 times in both cases. The porosity (*P*) was

calculated as the ratio between tapped density (ρ_b) and skeletal density (ρ_s) by the following equation[46]:

$$P = 1 - \left(\frac{\rho_b}{\rho_s}\right)$$

The BET surface area, external surface area, micropore surface area and micropore volume of the beads were measured by means of N_2 adsorption/desorption isotherm analysis using a 3Flex Physisorption Analyzer from MICROMERITICS at 77.3 K with a relative pressure (p/p_0) range of 10^{-9}–0.3 (RF) or 10^{-9}–0.4 (carbon). The micropore size distributions for carbon beads were calculated with original density functional theory using a N_2-DFT model. RF beads were outgassed at 120 °C for 12 h and carbon beads were outgassed at 200 °C for 12 h with a Smart VacPrep 067 HIVAC, MICROMERITICS before starting the measurements. The IUPAC recommendations for the application of the BET method to microporous materials has been taken in consideration for all measurements.[74]

ATR-IR spectroscopy was performed on a Tensor 27 spectrometer from BRUKER with a resolution of 4 cm^{-1} and 150 scans for each sample over the range of 4000–400 cm^{-1}.

Wide angle X-ray scattering (WAXS) measurements have been performed on a BRUKER D8 Advance diffractometer with Cu K_α radiation (λ = 1.5406 Å) at 35 kV and 30 mA. Beads were ground with an agate mortar and the powder was placed in a Si single crystal with a pit of 5 mm diameter and 0.8 mm depth. Raw data was processed with the EVA-program and the data was compared to the ICDD-PDF2 database (2019) and the BRUKER COD (2020).

The microstructures of the samples were analyzed using an ULTRA55 scanning electron microscope (SEM) from ZEISS with an operating voltage of 2 kV. A thin platinum layer was sputtered with a BAL-TEC SCD 500 Sputter Coater on all samples from the top for 60 s and with a current of 21 mA. RF beads were additionally being sputtered on from two opposite sites for 45 s and with a current of 21 mA before the measurements.

The surface tensions of RF sols with varying XG concentrations have been measured with a KRÜSSE force tensiometer K100 using the Du-Noüy method.

3.3 Preparation of RF and Carbon Aerogel Microbeads

In a typical synthesis, resorcinol (R) and deionized water (W) were first weighed into a 100 mL screw lid container. After 10 min of stirring with a magnetic stirring bar at 250 rpm, formaldehyde (F) solution (23.5%) was added and further stirred for another 10 min at 250 rpm before xanthan gum (XG) was added. Na_2CO_3 (C) was added as catalyst after the complete dispersion of XG. The initial pH value was ranging between 5.8–6.1 after further stirring for 40 min. In case of adjusting the pH value, HNO_3 (2M) was added with a micro pipette 10 minutes after Na_2CO_3 addition until the pH value was ranging between 5.4–5.6. The containers were closed airtight and placed into an oven at a preset temperature of 60 °C for pre-gelation. When the RF sol reached near the gelation point (determined based on trial), the container was taken out of the oven and cooled down in a water bath.

In order to produce microbeads, the RF sol was filled into a syringe or a pressurized container with multiple cannulas and dropped into the acid gelation bath. Blunt B.BRAUN Sterican cannulas with a length of 22 mm and a diameter of 0.8 mm have been used. The beads were left in the gelation bath until a color change to pink occured before being filtered and placed in a closed container in the oven at 60 °C for 1 d for further curing. After that all beads were washed with deionized water until neutral pH was achieved and then dried in an oven at 60 °C for at least 1–2 days. The following reactant ratios were used throughout the experiments: R/C=1500, R/F=0.74 and R/W=0.044 with a total mass concentration (M_{RF}) of 27%.

Carbonization was performed with following parameters using a GERO tube furnace with a maximum temperature of 1350 °C, a diameter of 150 mm and a length of 500 mm. The samples were heated to 1000 °C with 400 K/h and held for 1 h at 50 mbar under Ar atmosphere.

RF- and carbon microbeads were labelled as RFB and CB, respectively. In case of pH adjustment with HNO_3 (2M) “a” is used as suffix. Xanthan gum addition is noted with ‘XG’ and the respective concentration (wt.%) is added as prefix to XG. The gelation baths were referred as ‘H’ for hydrochloric acid and ‘N’ for nitric acid.

4. Results and Discussion

4.1 Dropping Process Development

In the following section, the improvements and insights concerning the process of RF aerogel bead production by dropping experiments are described and discussed.

Ratios of R/C = 1500, R/W = 0.044 and R/F = 0.74 have been chosen since the resulting materials have been successfully used for foundry applications[8a] and in preliminary experiments[73]. Furthermore a high R/C ratio of 1500 allows ambient drying at elevated temperatures without significant shrinkage of the gels.[75] The pH adjustment of the RF sol with 0.5M HNO_3 to a value of 5.4–5.6 is used, since RF aerogel granules produced with pH adjustment provided better sand core performance for foundries in the previous experiments from our group. Samples w/o pH adjustment have been produced for comparison.

As described in the experimental section, R was first dissolved in W followed by addition of F. After that XG was dispersed. The time required for complete dispersion of XG was depending on various parameters like beaker size, stirring speed, desired XG concentration and total sol amount. To prevent ongoing pre-gelation during XG dispersion which would lead to a less reproducible process, C was only added after XG was completely dispersed. Table 1 shows some example pre-gelation times of RFB- and RFBa sols pre-gelled at 60 °C containing various XG concentrations.

Table 1: Exemplary pre-gelation time of RFB- and RFBa sol at 60 °C.

XG conc. [w/v%]	RFB Time at 60 °C [min]	RFBa Time at 60 °C [min]
0	192	235
0.2	155	159
0.4	92	133
0.6	90	134
0.8	85	127
1	84	109

The pre-gelation time was generally reduced with increasing XG concentrations. Furthermore, RFBa sols generally required longer pre-gelation times than RFB sols. These pre-gelation times can nevertheless vary strongly since they also depend on the type of oven used, filling of the oven and position of the container in the oven (Fig. 21).

Figure 21: Varying pre-gelation progress of RFB sols after 58 min at 60 °C. Containers are placed on various positions.

All sols gradually turned from clear colorless in the beginning over clear pale yellow to clear orange and finally to slightly orange milky sols with increasing pre-gelation time. The optimal pre-gelation time for each sample was determined as the point when the sol just became milky. Sols with XG concentrations >0.6 wt.% had to be taken out shortly before the sol became milky, since they gelled during cooling in a water bath if taken out when already milky.

First dropping experiments have been conducted with one 20 ml syringe and one cannula (Fig. 22a). After that two syringes have been used simultaneously (Fig. 22b). These two methods were rather time- and labor consuming. The process has been significantly improved in terms of upscaling and time efficiency by using a pressurized vessel that contained 5 cannulas (Fig. 22c). The cannulas were pushed through holes in the lid of a screw lid container and the Ar-gas needle was pushed through a septum on the bottom of the container. An amount of 80 ml of sol with high XG content could be dropped in approx. 15 min instead of approx. 60 min for one syringe. This process had to be performed carefully since small changes in the pressure led to extrusion instead of dropping. The gas pressure had to be adjusted manually during the whole process.

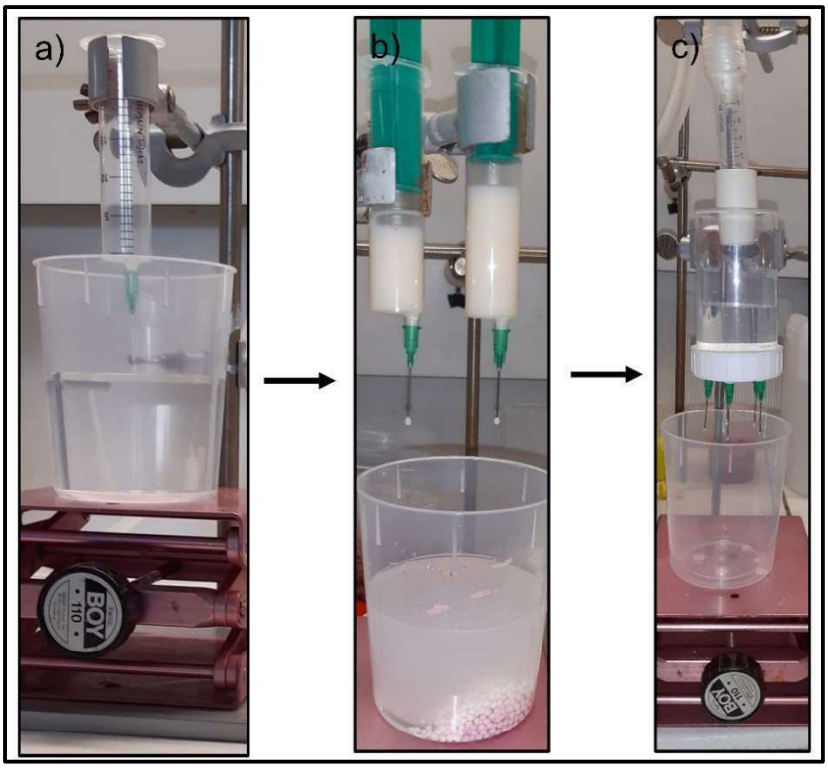

Figure 22: Photographs of dropping experiment setups with a) one syringe, b) two syringes and c) a pressurized container with 5 cannulas.

The dropping distance required to obtain spherical beads was increased with the XG concentration. Whilst a distance of 2 cm was required in a syringe dropping experiment with sol that contained 0.1% XG, 80 cm were required for a sol with 1.0% XG. When the pressurized multi-nozzle system was used, dropping distances as low as 5-10 cm were sufficient even for sols that contained 1.0% XG. Chan et al. have investigated the Ca-alginate bead formation mechanism during dropping experiments.[76] The shape of the resulting bead and the dropping distance were mainly determined by the viscosity, density and surface tension of the alginate solution. When the droplet detached from the nozzle, the shape was evolving from tear- to sphere shaped due to the surface tension effect. For solutions with higher viscosities a longer distance was needed for the droplet to become spherical. Furthermore, the droplets were deformed if the viscous-surface tension forces were not high enough to counteract the impact-drag forces when hitting and entering the gelation bath. A spherical droplet could also be deformed due to high impact-drag forces if the dropping distance became too high. Table 2 shows the surface tensions measured for XG containing pre-gelled RF sols typically used in this work.

Table 2: Surface tensions measured for pre-gelled RFB-XG solutions with varying XG concentrations.

XG conc. [w/v%]	Surface tension [mN/m]
0.0	55.1
0.2	58.1
0.4	59.8
0.6	60.5
0.8	60.0
1.0	59.9

XG containing sols have surface tensions ranging from 58-60 mN/m and sol w/o XG has a surface tension of 55 mN/m. The increase in the surface tension and viscosity for increasing XG concentrations explains why sols w/o XG resulted in flakes while sols with XG resulted in beads.

In preliminary experiments, 2M HCl has primarily been used as gelation bath. Other concentrations have been used to possibly improve the process time in case of higher concentrations or to possibly reduce the acid usage and thus the generated amount of waste. The beads were typically filtered when they turned from white to pink, since they were rigid enough at this point to prevent agglomeration upon filtration (Fig. 23). When placed in the oven, the color of the beads became more intense and turned to dark pink with a red undertone. A small amount of configurationally locked *o*-quinone methide or its spiro derivative are responsible for the red color in acid catalyzed RF aerogels.[77]

Figure 23: Color of RF aerogel microbeads: a) right after dropping and b) filtered after few minutes in the gelation bath.

Figure 24 shows the time until color change to pink for various HCl gelation bath concentrations.

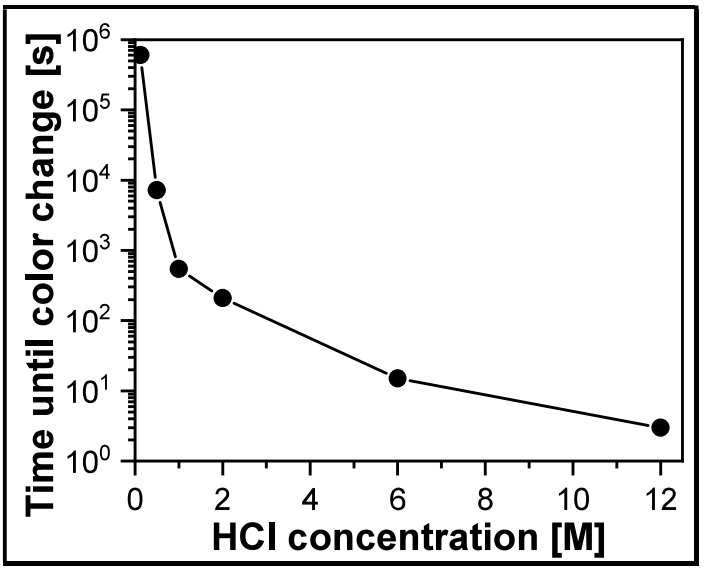

Figure 24: Time until the beads turned pink for HCl gelation baths with concentrations of 12.0M, 6.0M, 2.0M, 1.0M, 0.5M and 0.125M.

The time until color change was significantly reduced to a few seconds for HCl concentrations higher than 2M, but the bead size increased and became irregular since the acidic vapors lead to partial gelation at the cannula. For concentrations lower than 2M the time until color change increased drastically to a few days if the concentration was lower than 1M. Moreover, the beads had to be handled more carefully since they tended to agglomerate in the beaker and upon filtration. The use of 2M HCl as gelation bath offered best process time, bead stability upon handling and the acid amount.

In the case of using HNO_3 as gelation bath, a concentration as low as 0.5M had to be used since higher concentrations led to dissolution, nitration and oxidation of RF at elevated temperatures.[78] A 0.5M HNO_3 solution has a pH value of ~ 0.65 whilst a similar value is found for a 0.2M HCl solution. Even though the pH value of both acids is the same, the color change occurred much faster for HNO_3 (few minutes) than for HCl (1 day). Therefore, the reaction speed in the case of HCl and HNO_3 doesn't only depend on the pH value but also the type of acid used. At this point it is not clear which properties of the acids are responsible for this observation. More experiments should be performed in the future to investigate this effect.

During each dropping experiment, irrespective of the XG concentration, leaching of the beads started after they have been in the acid for a short time (Fig. 25). Since the leached-out material turns pink over time and yellow/orange after washing to pH-neutrality, it can be concluded that this material is composed of RF. It should be investigated, if XG is also leaching out.

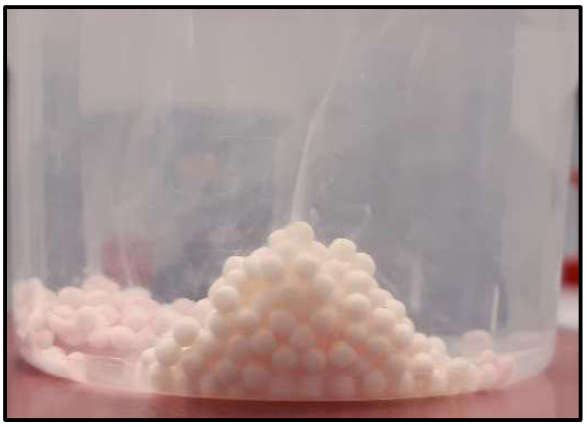

Figure 25: Photograph of leaching that was observed in each dropping experiment.

After curing in the oven, the beads have been washed to pH neutrality and filtered with a sieve (2.0 mm mesh) to separate the beads from the dust that was formed from the leaching. The bead color changed readily from pink to yellow/orange upon pH neutralization.

Furthermore, previously pre-gelled and frozen sol has successfully been used to produce RF beads even 10 weeks after pre-gelation of the sol (results not discussed/characterization not complete). By pre-gelling and freezing bigger amounts of sol, the dropping process can be performed more spontaneously and more time efficient, since a big amount of sol has to be pre-gelled only one time instead of pre-gelling freshly prepared sol every time an experiment must be performed.

4.2 RF Aerogel Beads without Xanthan Gum

In the frame of investigating the influence of XG addition on the dropping process and the resulting properties of XG containing beads, reference samples w/o the addition of XG have been produced. 2M HCl and 0.5M HNO_3 have been used as gelation baths for pre-gelled RF sol with and w/o pH adjustment. Figure 26 shows photographs of the resulting RFB samples w/o XG.

Figure 26: Photograph of RF aerogel flakes w/o XG.

The samples are brown/orange in color and have an irregular flake shape. The droplets couldn't withstand the impact upon entering the gelation bath and were therefore deformed before they gelled. Since only XG containing samples are of special interest in the framework of this work, the samples shown above have not been carbonized. Figure 27 shows the representative SEM overview and cross-section images of RFBa-H and RFBa-N.

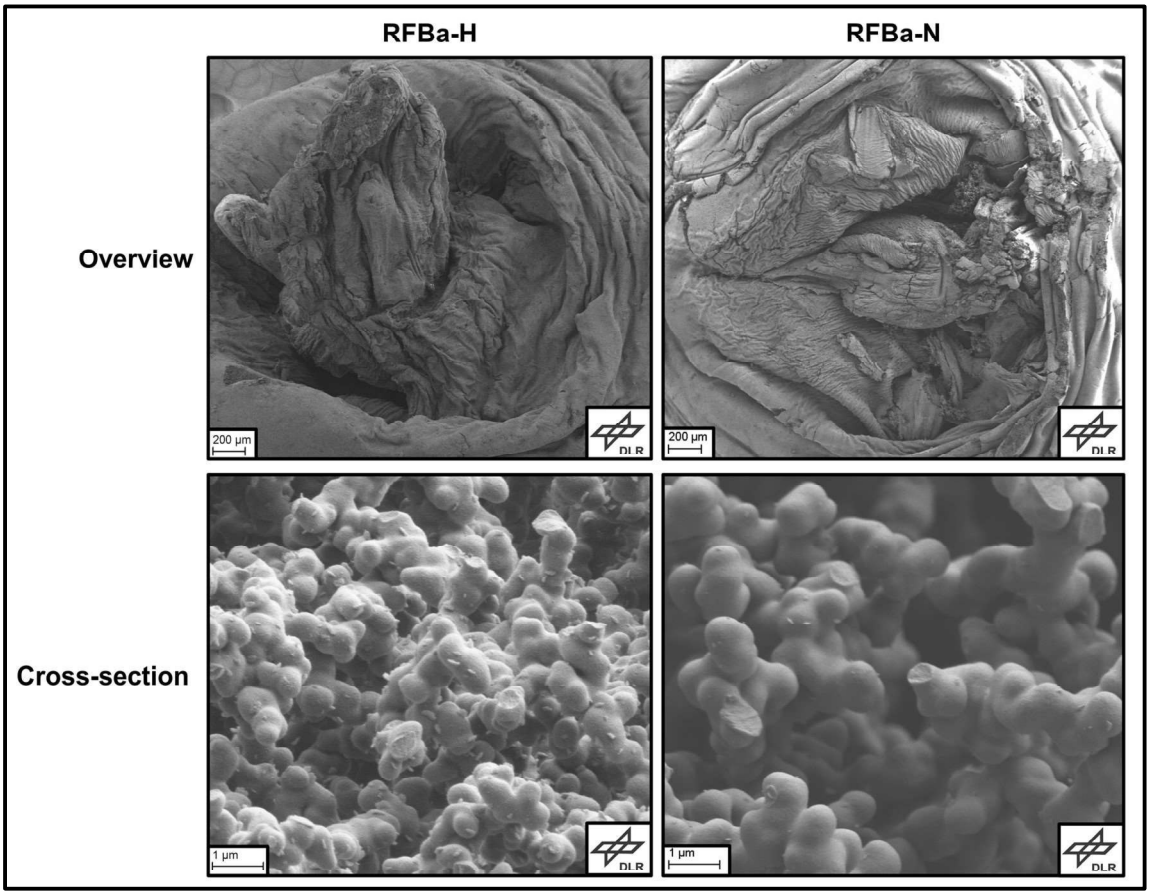

Figure 27: SEM overview and cross-section images of RFBa-H and RFBa-N.

The overview SEM images show wrinkled and unordered macroscopic structures. The microstructure of RFBa-H is composed of nearly spherical particles with sizes of approx. 0.5–0.7 µm while RFBa-N is composed of nearly spherical particles with sizes of approx. 0.7–1.0 µm. The connections between the particles are not clear and look covered. The samples furthermore exhibit micrometer sized macropores. Laskowski et al. have produced base-acid catalyzed monoliths of RF aerogel that show a similar microstructure.[15] The particle size was ranging between 50–2230 nm and decreased with longer pre-gelation time before the acid was added to the sol. The bigger particle size of RFBa-N might therefore result from small variations in the pre-gelation time before dropping the sol into the acid gelation bath. Furthermore, the

covering of the connections between particles was also observed by Laskowski et al. The remaining unreacted monomers reacted fast with pre-formed particles upon acid addition leading to an overall covering. Figure 28 shows the skeletal densities of RFB samples w/o XG.

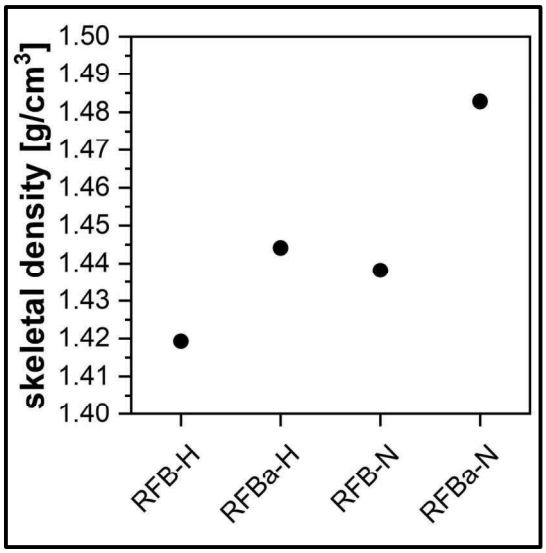

Figure 28: Skeletal densities of RFB-H, RFBa-H, RFB-N and RFBa-N.

The skeletal densities of RFB w/o XG are ranging between 1.42–1.48 g/cm^3, which is in accordance with values typically reported for RF aerogels.[15, 77] Figure 29 shows the BET surface areas of the RFB samples w/o XG.

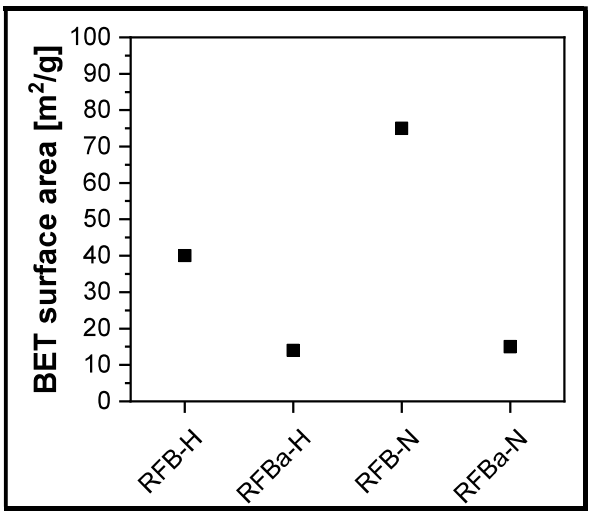

Figure 29: BET surface area of RFB-H, RFBa-H, RFB-N and RFBa-N.

The BET surface areas are ranging between 13–75 m^2/g. RFB-N (75 m^2/g) has a higher surface area than RFB-H (40 m^2/g). pH adjusted samples have, as expected for sols with lower pH values, a lower surface area in case of both gelation baths. Laskowski et al. reported specific surface areas as high as 97 m^2/g for base-acid

catalyzed RF aerogels. Since they used a much lower R/C ratio (R/C=200) for their synthesis, the surface area is as expected higher than for the samples shown above. Furthermore they observed, that the surface area is increasing for longer pre-gelation times.[15] Therefore small differences in the pre-gelation time of HCl and HNO_3 bath samples might have contributed to the differences in the surface area. Figure 30 shows the ATR-IR spectra of the above shown samples.

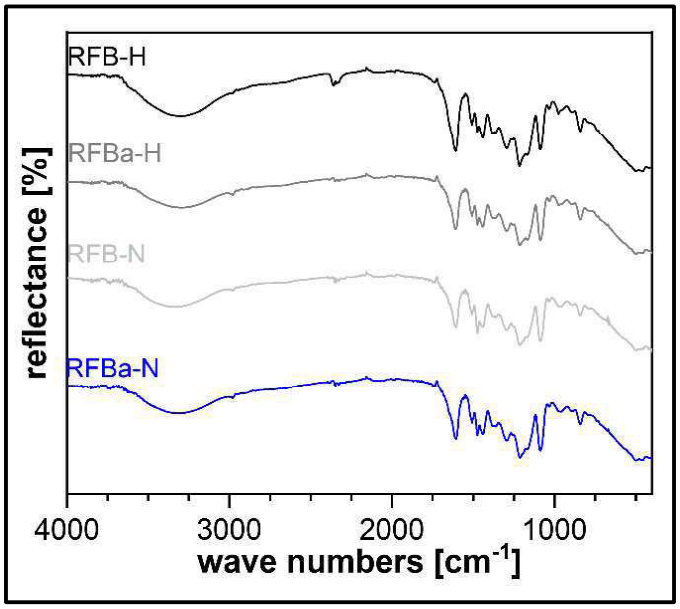

Figure 30: ATR-IR spectra of RFB samples w/o XG.

All obtained ATR-IR spectra have the same absorption bands regardless of pH adjustment or the acid used as gelation bath. The bands are furthermore in accordance with absorption bands reported by *Pekala* for base catalyzed RF aerogels[79] and by Mulik et al. for HCl catalyzed RF aerogels.[77] The band at 3382 cm^{-1} has been assigned to the -OH stretching vibration, the bands at 2942, 2874 and 1479 cm^{-1} have been assigned to the $-CH_2$ stretching and scissoring vibrations and the vibrations at 1222 and 1092 cm^{-1} have been assigned to the -C-O-C- stretching vibrations of methylene ether bridges.

Even though the microstructures, surface areas, skeletal densities and IR spectra were in accordance with values of RF aerogels reported in literature, the control of the shape and size of the beads was not given. Therefore, experimental series with varying XG concentrations for both acids and with or w/o pH adjustment were performed.

4.3 RF and Carbon Aerogel Beads with Xanthan Gum in HCl

RFB-XG-H samples have been produced with XG concentrations varying between 0.2–1.0% and were carbonized afterwards to obtain the respective CB-XG-H samples. Figure 31 shows photographs of resulting RFB-XG-H (left half) and CB-XG-H (right half) samples and a table with their respective carbonization yields.

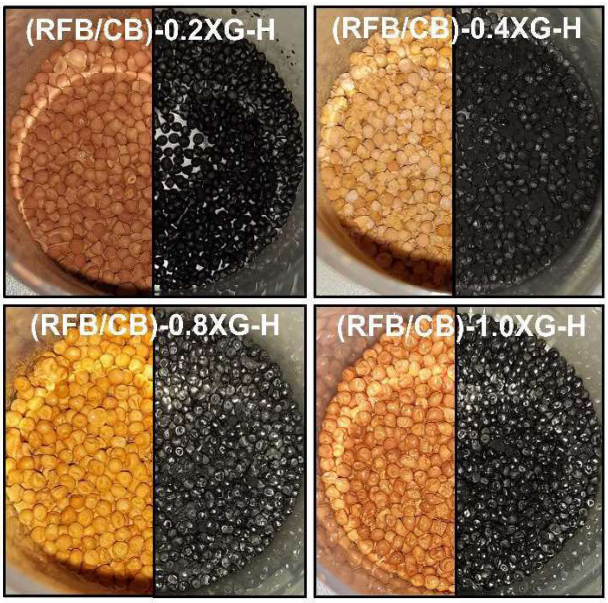

Sample	Carb. Yield [%]
0.2XG	42.8
0.4XG	45.8
0.6XG	35.3
0.8XG	41.4
1.0XG	43.2

Figure 31: Photographs of RFB-XG-H (left half) and CB-XG-H (right half) with varying XG concentrations. The carbonization yield is given as percentual mass ratio before and after carbonization.

The resulting RFB-XG-H samples appear brown/orange and are nearly spherical irrespective of the XG concentration. They were successfully carbonized with yields ranging between 35.3–45.8% (Fig. 31, table), resulting in black samples with similar shape. For RF aerogels w/o XG addition a carbonization yield of approx. 50% is reported in literature.[80] The additional weight loss for RFB-XG-H might result from additional functional groups added with XG or residual water in the pores. Table 3 gives the average size, standard deviation and vol. shrinkage of selected RFB-XG-H and CB-XG-H samples.

Table 3: Diameter and vol. shrinkage of RFB-XG-H and CB-XG-H with varying XG concentrations.

XG Conc. [w/v%]	RFB-XG-H [mm]	CB-XG-H [mm]	Vol. Shrinkage [%]
0.2	2.24±0.19	1.76±0.13	21.4
0.6	2.32±0.10	1.75±.0.08	24.6
1.0	2.56±0.25	2.02±0.20	21.1

The average RFB-XG-H size is increasing with the XG concentration from 2.24 mm (0.2% XG) over 2.32 mm (0.6% XG) to 2.56 mm (1.0% XG), but the standard deviations are rather high, resulting in overlapping size distributions. CB-XG-H samples generally have smaller sizes (1.75–2.02 mm) than their respective RFB precursors. The volumetric shrinkage after carbonization is ranging between 21.4–24.6%, which is in accordance with literature values.[81] Figure 32 shows overview SEM images of RFB-XG-H and CB-XG-H with varying XG concentrations.

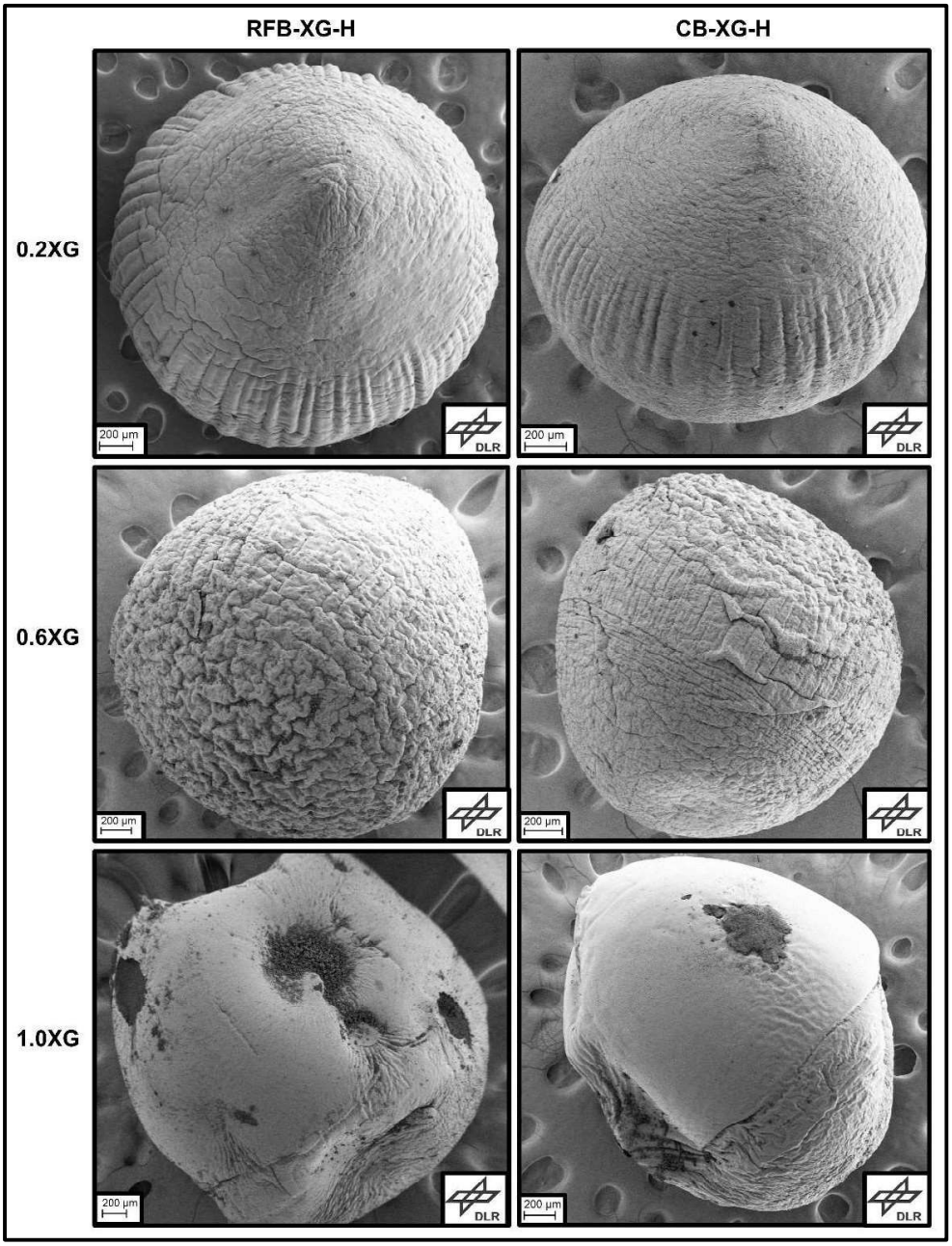

Figure 32: SEM images of RFB-XG-H (left) and CB-XG-H (right) with varying XG concentrations.

The SEM images reveal tear shaped beads for RFB-XG-H and CB-XG-H with 0.2% and 0.6% XG, while oblate like beads are obtained for RFB-1.0XG-H and CB-1.0XG-H. Those irregular shapes might be a result of adjusting the dropping distance throughout the dropping process. Furthermore, RFB-XG-H and CB-XG-H with 0.2% and 0.6% XG have a wrinkled surface while RFB-1.0XG-H and CB-1.0XG-H have dents. Figure 33 shows cross-sectional images of RFB-0.6XG-H and CB-0.6XG-H. Both samples have a dense skin which can be distinguished from the internal structure of the beads. Skin formation on RF and carbon aerogels is a known phenomenon.[82]

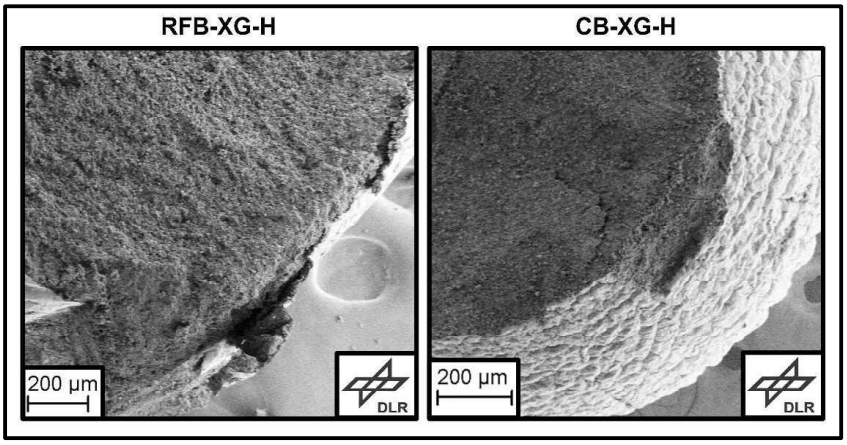

Figure 33: SEM images of RFB-0.6XG-H (left) and CB-0.6XG-H (right).

The wrinkled structure of the above shown beads might be a result from rapid gelation, sudden densification and therefore shrinkage of the surface. The dents in RFB-1.0XG-H and CB-1.0XG-H are a result of other beads lying on top during the gelation process. Since the SEM images only show single representative beads, wrinkling and dents might occur in all observed samples irrespective of the XG concentration.

The internal microstructures of the beads are shown in figure 34. The microstructure of all shown samples is again composed of nearly spherical particles whose connections look covered, which is in agreement of base-acid catalyzed RF aerogels[15] and carbon aerogels with same reactant ratios and carbonization conditions used here.[3] Particle sizes of few hundred nm and macropores with a size of few microns can be observed. CB-XG-H samples generally have a smaller particle size than their respective RFB-XG-H samples. RFB-0.6XG-H and RFB-1.0XG-H have bigger particles than RFB-0.2XG-H, which is probably a result of a small difference in the pre-gelation time.

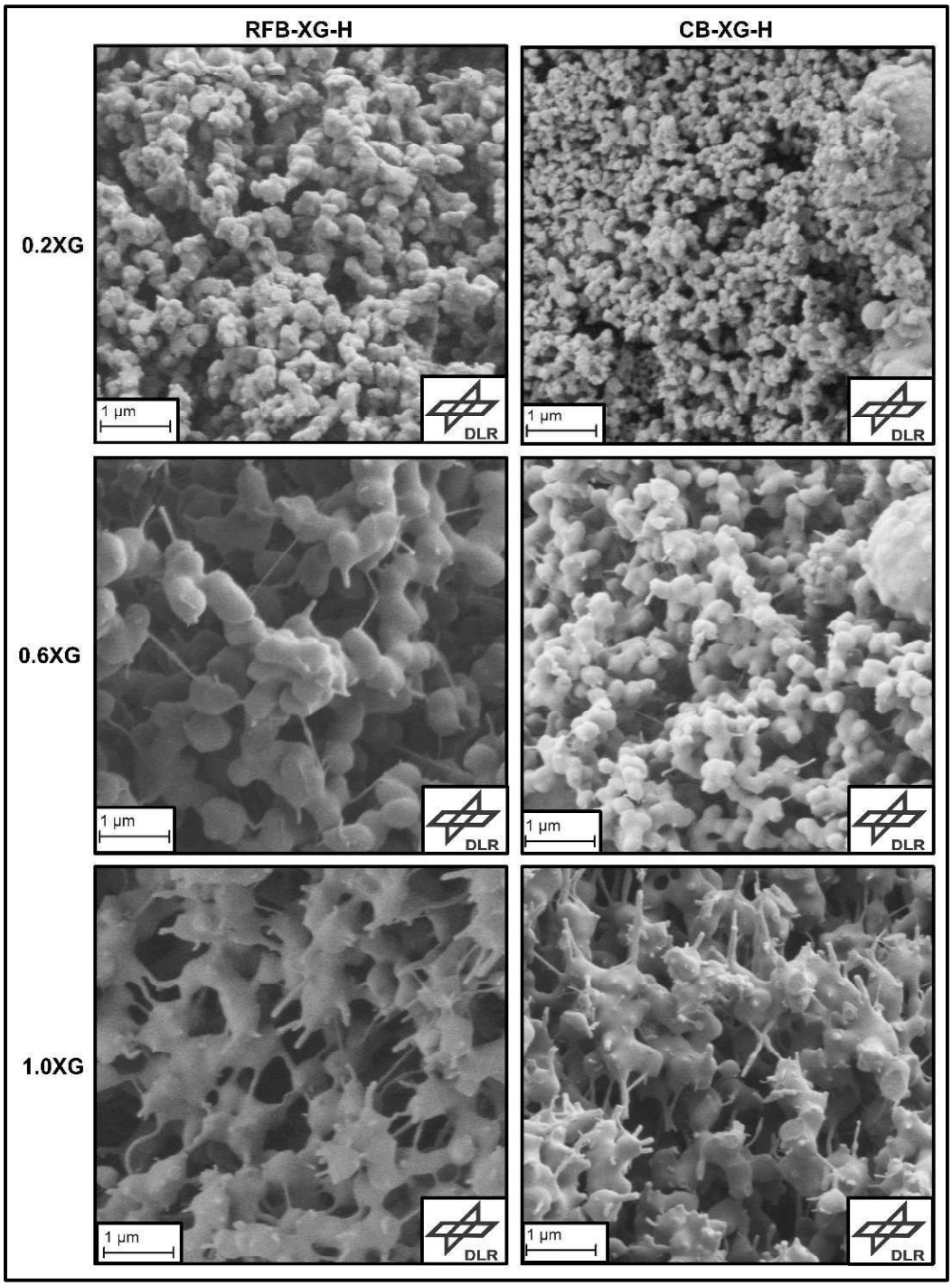

Figure 34: Cross-section SEM images of RFB-XG-H (left) and CB-XG-H (right) with varying XG concentrations.

One significant change with increasing XG concentrations is the appearance of fiber structures. The RF particles have grown on top of the fibers and are interconnected by them. The amount of fibers in RFB-XG-H is increasing with the XG concentration. The fiber structure is remained after carbonization. When XG is dispersed in water at pH values similar to the ones used during pre-gelation time in this work, fiber structures have been observed with an AFM method.[83] This fiber structure might be frozen even

after gelation because RF is growing on top and therefore prevents agglomeration. Furthermore, the reduced gelation time with increasing XG content might be explained by the interconnection of RF particles by XG fibers. Figure 35 shows the skeletal and tapped densities of RFB-XG-H and CB-XG-H with varying XG concentrations.

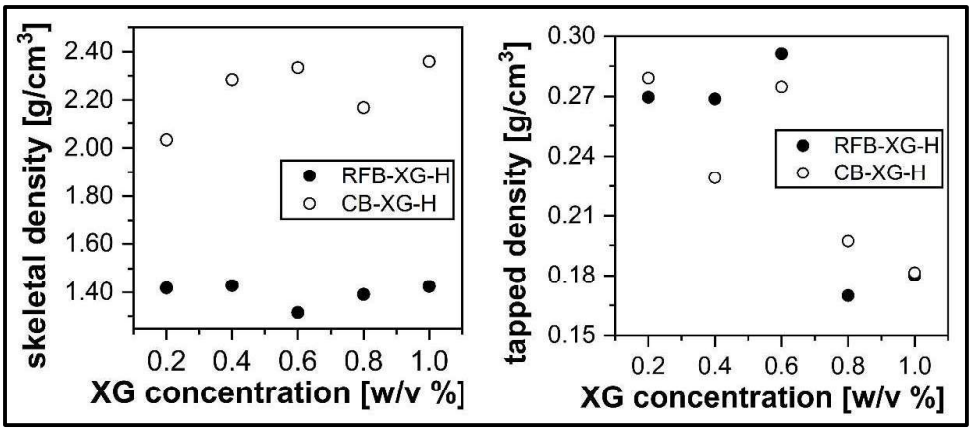

Figure 35: Skeletal- and tapping densities of RFB-XG-H and CB-XG-H with varying XG concentrations.

The skeletal densities of RFB-XG-H are with exception of RFB-0.6XG-H (1.32 g/cm^3) ranging between 1.39–1.42 g/cm^3, which are typical values for RF aerogels.[77] CB-XG-H has skeletal densities ranging from 2.0–2.4 g/cm^3 which is in accordance with skeletal densities of similar monolithic carbon aerogels.[3] The tapped densities of RFB-XG-H are ranging between 0.17–0.29 g/cm^3 and the tapped densities of CB-XG-H are ranging between 0.18–0.28 g/cm^3. The XG concentration has no influence on the tapped densities. The differences between the tapped densities are probably a result of differences in size and shape of the beads. Bulk densities of monolithic RF aerogels produced with base-acid catalysis are ranging between 0.24–0.32 g/cm^3.[15] For monolithic carbon aerogels a bulk density of 0.34 g/cm^3 is reported.[84] Table 4 shows the resulting porosities of RFB-XG-H and CB-XG-H.

Table 4: Porosities of RFB-XG-H and CB-XG-H with varying XG concentrations.

XG conc. [w/v%]	RFB-XG-H Porosity [%]	CB-XG-H Porosity [%]
0.2	81	86
0.4	84	90
0.6	78	88
0.8	88	91
1.0	87	92

The porosities of RFB-XG-H are ranging between 78–88% and the porosities of CB-XG-H are ranging between 86–92%. The XG concentration has no influence on the porosity. CB-XG-H samples have a higher porosity than their RFB-XG-H precursors.

The representative sorption isotherms of RFB and CB samples are shown in figure 36. The sorption isotherms of the prepared RFB exhibit a combination of type II and type IV isotherm character, indicating the presence of macropores (seen in SEM images shown below).[74, 77] The prepared CB exhibits a combination of strong type I isotherm character of microporous materials with little contribution of type IV isotherm character of mesoporous materials.[3, 74] The micropore volume increased from almost no micropores for RFB-0.1XG-H to 0.36 cm^3/g in CB-0.1XG-H upon carbonization. The micropore and external surface area of CB-0.1XG-H were found to be 931 and 93 m^2/g respectively. Since approx. 90% of the surface area comes from micropores, further analysis was focused on micropore characteristics of each CB sample.

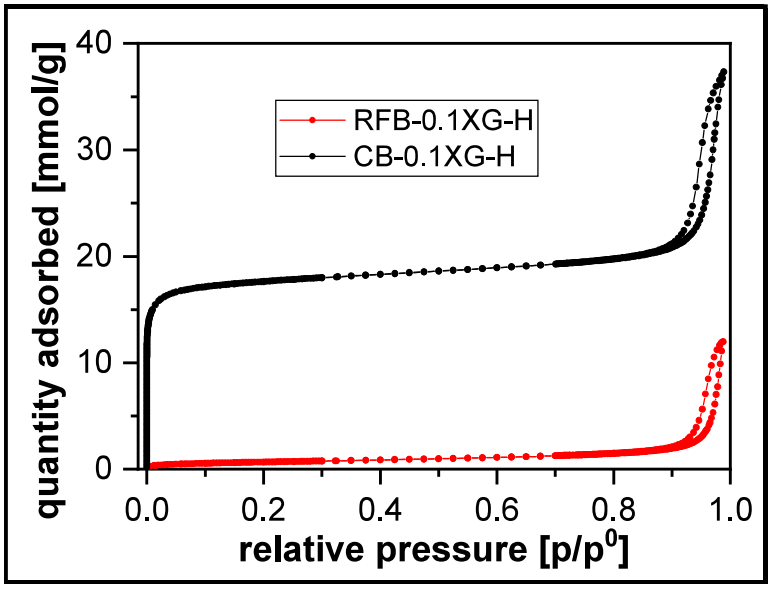

Figure 36: Nitrogen sorption isotherms of RFB-0.1XG-H and CB-0.1XG-H.

Figure 37 shows the BET surface area of RFB-XG-H and CB-XG-H with varying XG concentrations.

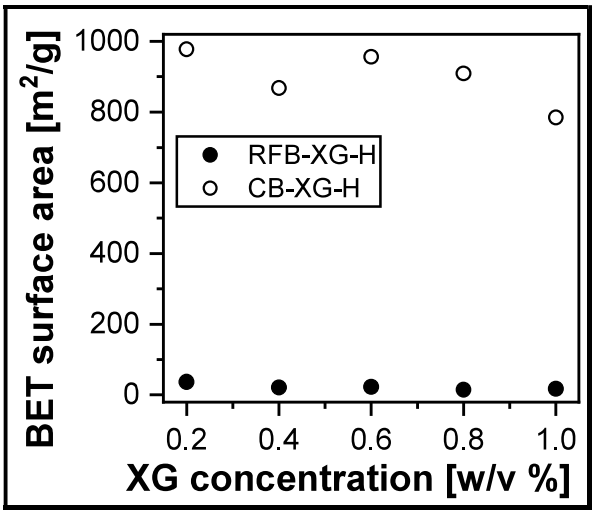

Figure 37: BET surface area of RFB-XG-H and CB-XG-H with varying XG concentrations.

The BET surface area of RFB-XG-H samples is ranging between 15–37 m^2/g and in the same region like RFB-H and other base-acid catalyzed RF aerogels.[15] The BET surface area of CB-XG-H is ranging between 785–978 m^2/g and similar to other carbon aerogels.[3, 85] Carbon aerogels have a much higher surface area than RF aerogels due to the formation of micropores during carbonization.[85] The XG concentration has no significant influence on the surface area of RFB-XG-H and CB-XG-H. Table 5 shows the external- and micropore surface area and micropore volumes of CB-XG-H.

Table 5: External- and micropore surface area and micropore volume for CB-XG-H.

Sample	External Surface Area [m^2/g]	Micropore Surface Area [m^2/g]	Micropore Volume [cm^3/g]
CB-0.2XG-H	77	901	0.35
CB-0.4XG-H	84	784	0.30
CB-0.6XG-H	95	861	0.33
CB-0.8XG-H	62	847	0.33
CB-1.0XG-H	50	735	0.28

The ratio of external- and micropore surface area reveals a dominating content of micropores in CB-XG-H irrespective of the XG concentration. 735–901 m^2/g of the surface area result from micropores while only 50–95 m^2/g result from the external surface of the beads. The micropore volume is ranging from 0.28–0.35 cm^3/g and also not correlating with the XG-concentration. The micropore volume of similar carbon aerogels is ranging between 0.20–0.22 g/cm^3.[3] Figure 38 shows the DFT calculated pore size distribution of CB-XG-H with varying XG concentrations.

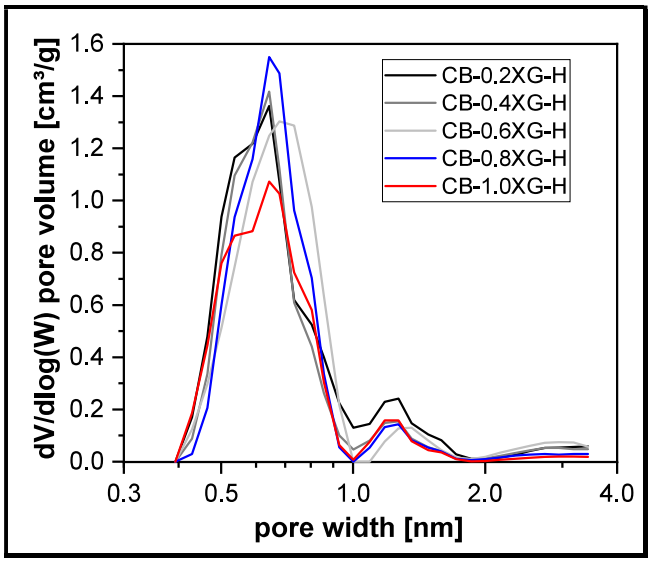

Figure 38: Micropore size distribution of CB-XG-H with varying XG concentrations calculated by N_2-DFT Model.

All samples show a high amount of micropores with widths ranging between 0.4–1.0 nm and additional pores with sizes slightly above 1.0 nm. The XG concentration doesn't influence the micropore size distributions of CB-XG-H. The micropore size of similar carbon aerogels is ranging between 0.5–2.0 nm.[3]

Figure 39 shows the ATR-IR spectra of RFB-XG-H and CB-XG-H samples. All obtained ATR-IR spectra of RFB-XG-H have the same absorption bands regardless of the XG concentration and are in accordance with literature spectra.[77, 79] A XG reference spectrum shows absorption bands at 3309, 1606, 1400, 1370, 1238 and 1016 cm^{-1}, which is in accordance with literature spectra.[86] Since both, RF and carbohydrates in general contain of methylene groups and aliphatic alcohols, the absorption bands are overlapping. Nevertheless, XG has a band at 1016 cm^{-1} (deformation of C-O) which doesn't overlap with the RF spectrum and doesn't appear in the RFB-XG-H spectra. A concentration of 1.0% might be too low to observe the bands of XG in RFB-XG-H spectra. As seen in the SEM images, RF grows on top of XG. It is therefore concluded from ATR-IR spectra that the addition of XG additive does not influence or hinder the polycondensation of the precursors and thus the formation of RF aerogel. The CB-XG-H samples show only a general low reflectance without sharp absorption bands. It is therefore concluded that CB samples don't contain any residual functional groups from RF or XG.

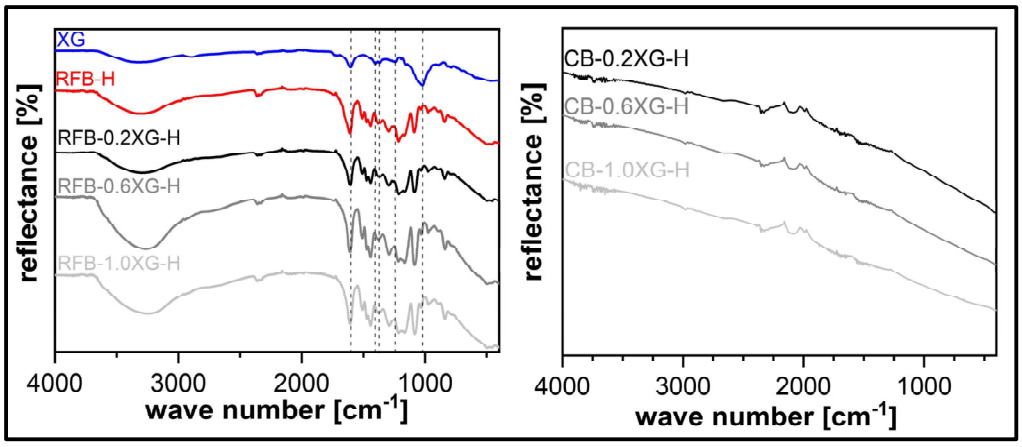

Figure 39: ATR-IR spectra of RFB-XG-H (left) and CB-XG-H (right) with varying XG concentrations. XG reference spectrum is added.

Figure 40 shows the WAXS pattern of CB0.6XG-H.

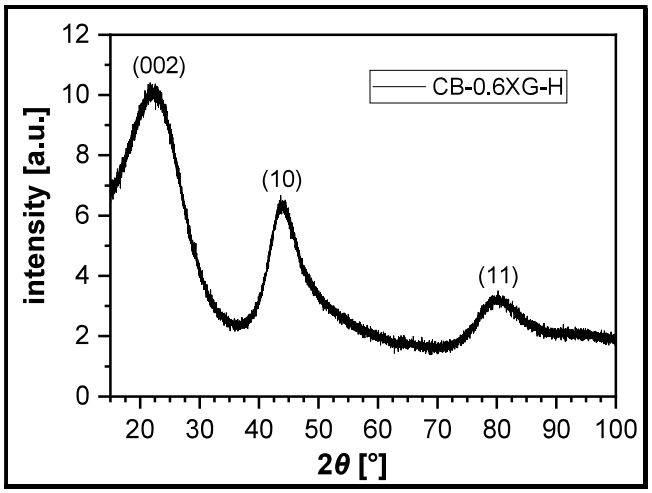

Figure 40: WAXS pattern of CB-0.6XG-H.

The above shown diffractogram shows peaks at 22.4° (002), 43.7° (10) and 79.9° (11) which are in accordance with literature diffractograms of carbon aerogels.[3, 87] The (002) reflex result from interlayer scattering between parallel stacked layers and the (10) and (11) reflexes result from intralayer scatterings within the graphene layers. The wideness of the peaks is typical for nanocrystalline turbostratic carbons.[3]

In this section it was shown, that the addition of XG resulted in a much smoother dropping process which led to spherical-like RFB-XG-H and CB-XG-H. Increasing XG concentration resulted in larger beads, shorter gelation times and a fibrous network on which RF grew while other properties like the densities, surface areas and IR spectra were not significantly influenced by the addition of XG.

4.4 RF and Carbon Aerogel Beads with Xanthan Gum in HCl – pH adjustment

RFBa-XG-H samples have been produced with XG concentrations varying between 0.2–1.0% and were carbonized afterwards to obtain CBa-XG-H. The pH-value was adjusted to 5.4–5.6 with HNO_3 (0.5M). Figure 41 shows photographs of resulting RFBa-XG-H (left) and CBa-XG-H (right) samples and a table with their respective carbonization yields.

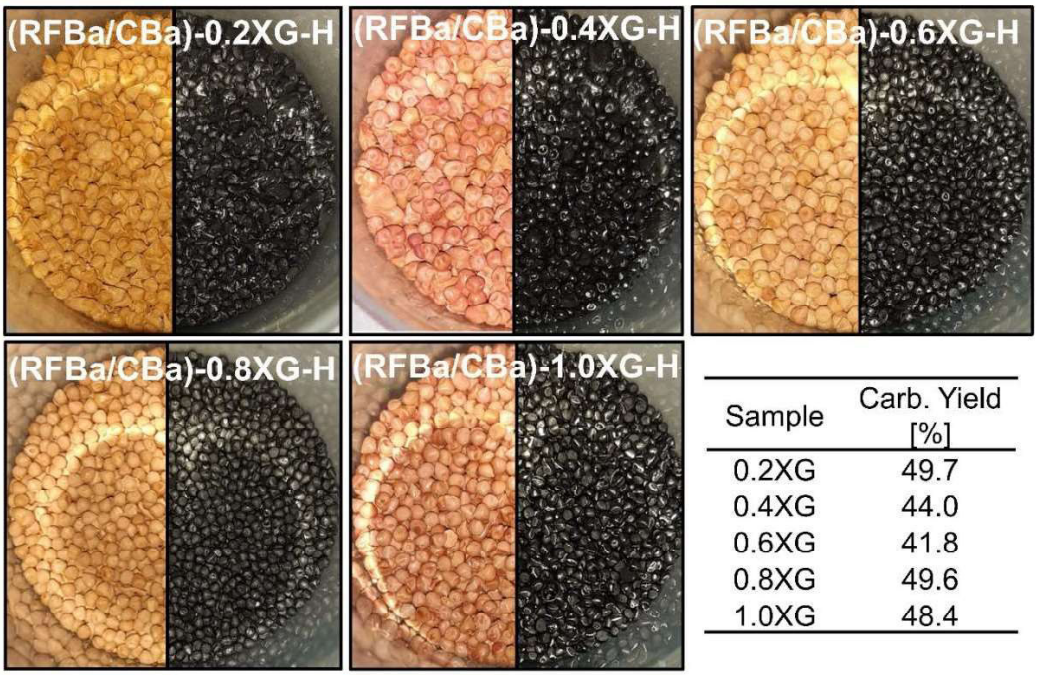

Sample	Carb. Yield [%]
0.2XG	49.7
0.4XG	44.0
0.6XG	41.8
0.8XG	49.6
1.0XG	48.4

Figure 41: Photographs of RFBa-XG-H (left half) and CBa-XG-H (right half) with varying XG concentrations. The carbonization yield is given as mass ratio before and after carbonization.

The resulting RFBa-XG-H samples similar to RFB-XG-H appear brown/orange and are nearly spherical irrespective of the XG concentration. CBa-XG-H could be obtained with carbonization yields ranging between 41.8–49.7% (Fig. 40, table), which is slightly higher than for RFB-XG-H but otherwise in accordance with literature values.[80] CBa-XG-H samples are black and have a shape like their RFBa-XG-H precursors. Table 6 gives the average size, standard deviation and vol. shrinkage of selected RFBa-XG-H and CBa-XG-H.

Table 6: Diameter and vol. shrinkage of RFBa-XG-H and CBa-XG-H with varying XG concentrations.

XG conc. [w/v%]	RFBa-XG-H [mm]	CBa-XG-H [mm]	Vol. Shrinkage [%]
0.2	2.18±0.26	1.80±0.11	17.4
0.6	2.35±0.16	1.85±0.16	21.3
1.0	2.41±0.17	1.88±0.13	22.0

The average RFBa-XG-H size is increasing with the XG concentration from 2.18 mm (0.2% XG) over 2.35 mm (0.6% XG) to 2.41 mm (1.0% XG), but the standard deviations are rather high, resulting in overlapping size distributions. CBa-XG-H samples generally have smaller sizes (1.80–1.88 mm) than their precursors. The volumetric shrinkage after carbonization is ranging between 17.4–22.0%, which is in accordance with literature values.[81] The bead sizes are similar to RFB-XG-H and CB-XG-H. Figure 42 shows overview SEM images of RFBa-XG-H and CBa-XG-H with varying XG concentrations.

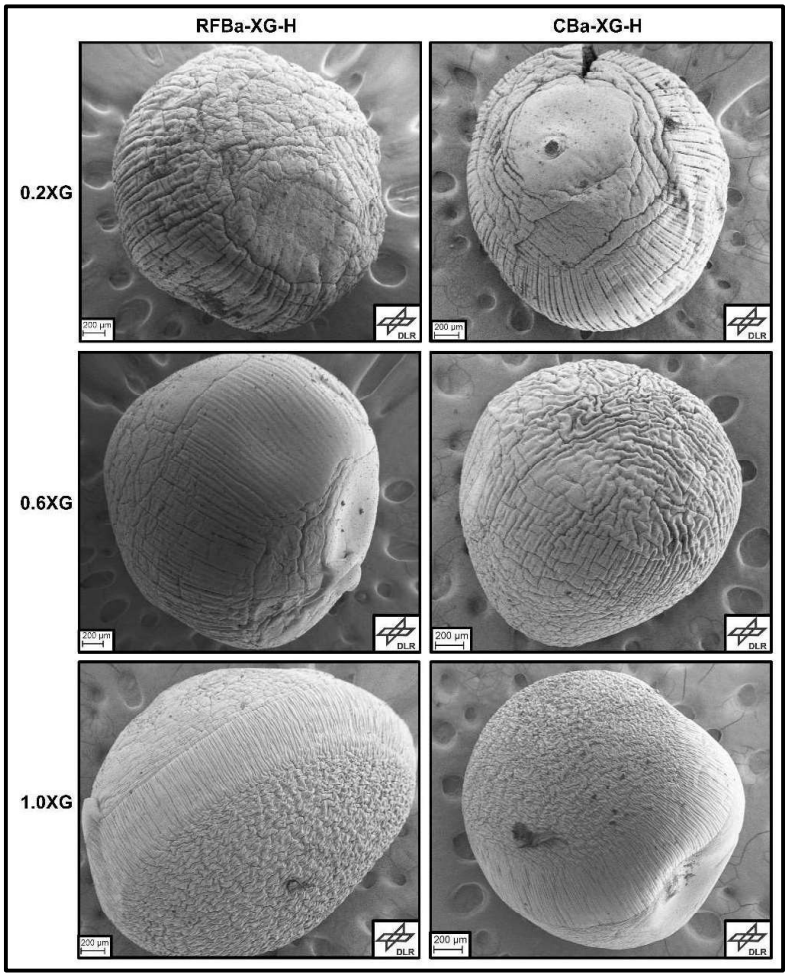

Figure 42: SEM images of RFBa-XG-H (left) and CBa-XG-H (right) with varying XG concentrations.

The SEM images reveal tear- and oblate shaped beads with wrinkled surfaces and dents. The internal microstructures of the beads are shown in figure 43. The microstructure of all shown samples is again composed of nearly spherical particles whose connections look covered, which is in agreement with literature.[3, 15] Particle sizes of few hundred nm and macropores with a size of few microns can be observed. The CBa-XG-H samples generally have a smaller particle size than their respective RFBa-XG-H samples. In RFBa-0.6XG-H and CBa-0.6XG-H few big particles with a size in the micron region can be seen. For higher XG concentrations fibers on which the RF has grown can be seen again. There are no other significant differences compared to RFB-XG-H and CB-XG-H samples.

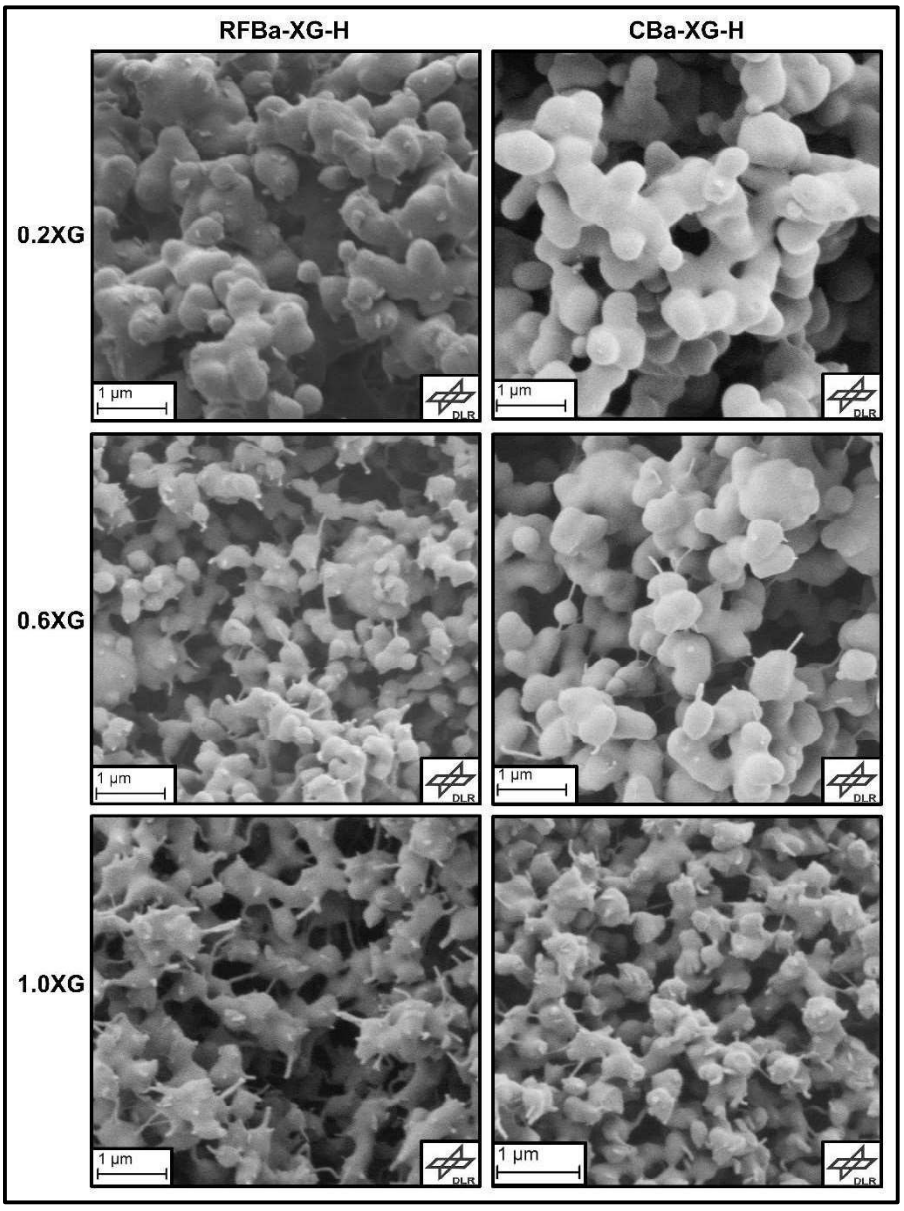

Figure 43: Cross-section SEM images of RFBa-XG-H (left) and CBa-XG-H (right) with varying XG concentrations.

Figure 44 shows the skeletal densities and tapped densities of RFBa-XG-H and CBa-XG-H with varying XG concentrations.

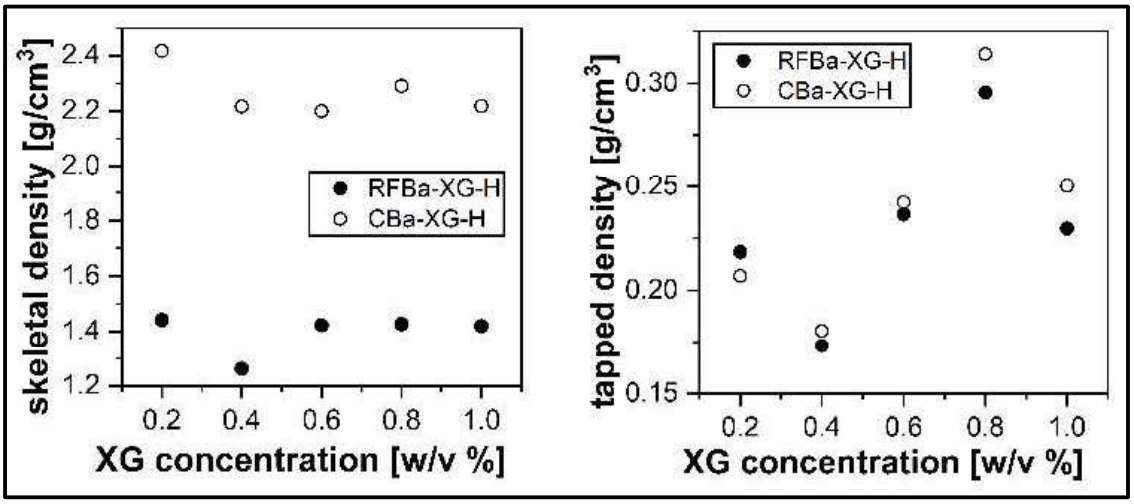

Figure 44: Skeletal- and tapped densities of RFBa-XG-H and CBa-XG-H with varying XG concentrations.

The skeletal densities of RFBa-XG-H are, with the exception of RFBa-0.4XG-H (1.26 g/cm^3), ranging between 1.42–1.44 g/cm^3, which are typical values for RF aerogels.[77] CBa-XG-H has skeletal densities ranging from 2.20–2.42 g/cm^3 which is in accordance with values reported in literature.[3] The tapped densities of RFBa-XG-H are ranging between 0.17–0.30 g/cm^3 and 0.18–0.31 g/cm^3 for CBa-XG-H. The densities are similar to the values for RFB-XG-H and CB-XG-H and don't correlate with the XG concentration. Table 7 shows the resulting porosities of RFBa-XG-H and CBa-XG-H.

Table 7: Porosities of RFBa-XG-H and CBa-XG-H with varying XG concentrations.

XG conc. [w/v%]	RFBa-XG-H Porosity [%]	CBa-XG-H Porosity [%]
0.2	85	91
0.4	86	92
0.6	83	89
0.8	79	86
1.0	84	89

The porosities of RFBa-XG-H are ranging between 79–86% and the porosities of CBa-XG-H are ranging between 86–92%. CBa-XG-H samples have a higher porosity than their corresponding RFBa-XG-H samples. The porosities are in the same

region like for RFB-XG-H and CB-XG-H. Figure 45 shows the BET surface area of RFBa-XG-H and CBa-XG-H with varying XG concentrations.

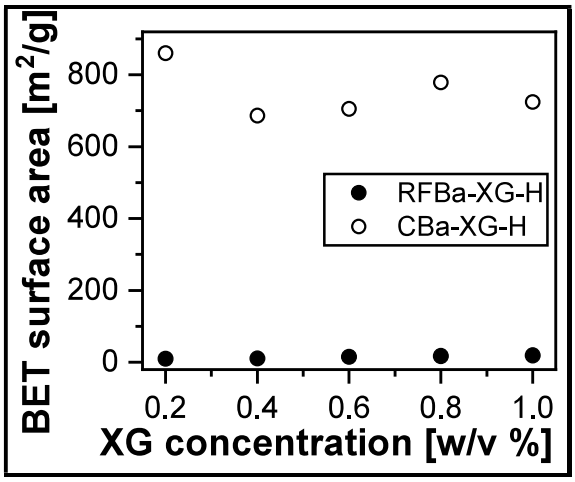

Figure 45: BET surface area of RFBa-XG-H and CBa-XG-H with varying XG concentrations.

The BET surface area of RFBa-XG-H is ranging between 9–19 m^2/g and between 687–860 m^2/g for CBa-XG-H. The surface areas are not directly correlating with the XG concentration and are lower than for RFB-XG-H (15–37 m^2/g) and CB-XG-H (785–978 m^2/g). Table 8 shows the external- and micropore surface area and micropore volumes of CBa-XG-H.

Table 8: External- and micropore surface area and micropore volume for CBa-XG-H.

Sample	External Surface Area [m^2/g]	Micropore Area [m^2/g]	Micropore Volume [cm^3/g]
CBa-0.2XG-H	53	807	0.31
CBa-0.4XG-H	41	646	0.25
CBa-0.6XG-H	55	651	0.25
CBa-0.8XG-H	63	716	0.27
CBa-1.0XG-H	57	668	0.26

The ratio of external- and micropore surface area reveals a dominating content of micropores in CBa-XG-H irrespective of the XG concentration. 646–807 m^2/g of the surface result from micropores while only 41–63 m^2/g result from the external surface of the beads. The micropore volume is ranging from 0.25–0.31 cm^3/g and is also not correlating with the XG-concentration. The micropore area and micropore volume of CBa-XG-H samples is lower than for CB-XG-H samples (0.28–0.35 cm^3/g). Figure 46 shows the DFT calculated pore size distribution of CBa-XG-H with varying XG concentrations.

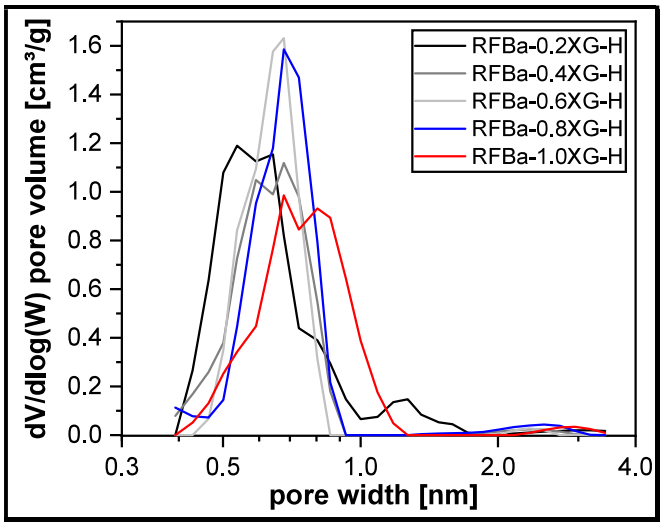

Figure 46: Micropore size distribution of CBa-XG-H with varying XG concentrations calculated by N_2-DFT Model.

All samples show a high amount of micropores with widths ranging between 0.4–1.0 nm. Only CBa-0.2XG-H and CBa-1.0XG-H show additional pores with sizes slightly above 1.0 nm. The XG concentration doesn't influence the micropore size distributions of CBa-XG-H. CBa-XG-H and CB-XG-H have similar micropore size distributions. Figure 47 shows the ATR-IR spectra of RFBa-XG-H and CBa-XG-H samples.

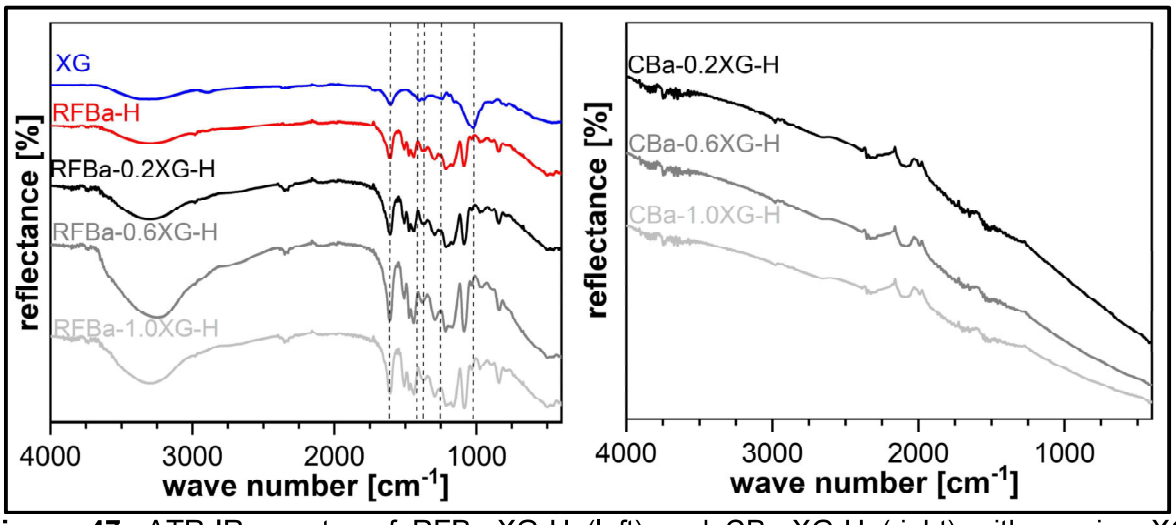

Figure 47: ATR-IR spectra of RFBa-XG-H (left) and CBa-XG-H (right) with varying XG concentrations. XG reference spectrum is added.

All obtained ATR-IR spectra of RFBa-XG-H have the same absorption bands regardless of the XG concentration and are in accordance with RFB-XG-H, and literature spectra.[77, 79] The CBa-XG-H samples show only a general low reflectance without sharp absorption bands. It is therefore concluded that CB samples don't

contain any residual functional groups from RF or XG. Figure 48 shows the WAXS pattern of CBa-0.6XG.H.

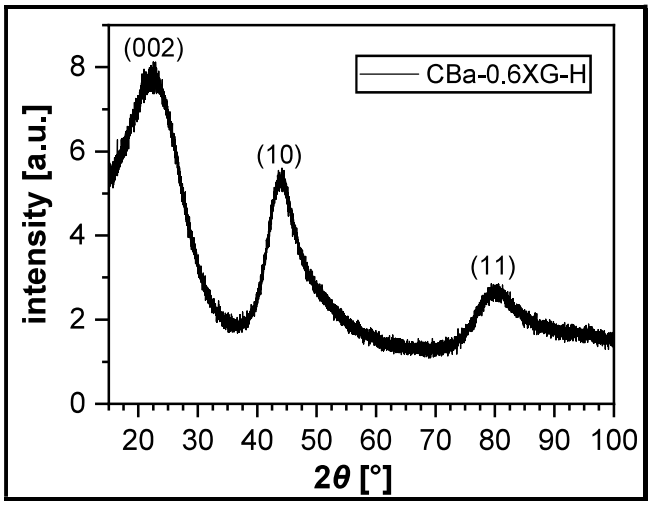

Figure 48: WAXS pattern of CBa-0.6XG-H.

The above shown diffractogram shows peaks at 22.2° (002), 44.0° (10) and 80.3° (11) which are in accordance with literature diffractograms of carbon aerogels. The wideness of the peaks is typical for nanocrystalline turbostratic carbons.[3, 87]

To summarize, increasing XG concentration only influences the bead size and the microstructure of RFBa-XG-H and CBa-XG-H. Furthermore, when RFBa-XG-H and CBa-XG-H are compared with RFB-XG-H and CB-XG-H, the only differences are a lower BET surface area and micropore volume of RFBa-XG-H and CBa-XG-H.

4.5 RF and Carbon Aerogel Beads with Xanthan Gum in HNO_3

RFB-XG-N samples have been produced with XG concentrations varying between 0.2–1.0% and were carbonized afterwards to obtain CB-XG-N. Figure 49 shows photographs of resulting RFB-XG-N (left half) and CB-XG-N (right half) samples and a table with their respective carbonization yields.

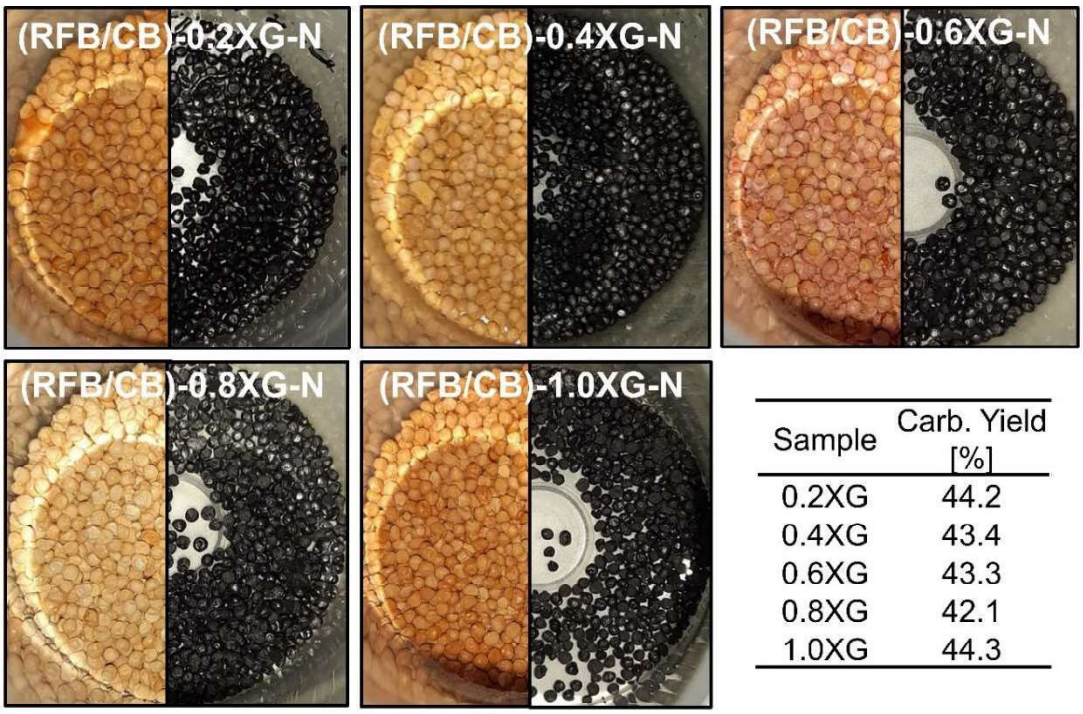

Sample	Carb. Yield [%]
0.2XG	44.2
0.4XG	43.4
0.6XG	43.3
0.8XG	42.1
1.0XG	44.3

Figure 49: Photographs of RFB-XG-N (left half) and CB-XG-N (right half) with varying XG concentrations. The carbonization yield is given as mass ratio before and after carbonization.

The resulting RFB-XG-N samples appear brown/orange and are nearly spherical irrespective of the XG concentration. CB-XG-N could be obtained with carbonization yields ranging between 42.1–44.3% (Fig. 48, table), which are similar to the samples shown in previous chapters. Table 9 gives the average size, standard deviation and vol. shrinkage of selected RFB-XG-N and CB-XG-N.

Table 9: Diameter and vol. shrinkage of RFB-XG-N and CB-XG-N with varying XG concentrations.

XG conc. [w/v%]	RFB-XG-N [mm]	CB-XG-N [mm]	Vol. Shrinkage [%]
0.2	2.37±0.16	1.86±0.14	21.5
0.6	2.36±0.16	1.77±0.18	25.0
1	2.22±0.23	1.66±0.17	25.2

The average RFB-XG-N size is decreasing with the XG concentration from 2.37 mm (0.2% XG) over 2.36 mm (0.6% XG) to 2.22 mm (1.0% XG), but the standard deviations are rather high, resulting in overlapping size distributions. CB-XG-N samples generally have smaller sizes than their respective RFB-XG-N precursors. The volumetric shrinkage after carbonization is ranging between 21.5–25.2%, which is in accordance with literature values.[81] The bead sizes are similar to samples discussed in previous chapters but with the main difference of decreasing with increasing XG concentration. Figure 50 shows overview SEM images of RFB-XG-N and CB-XG-N with varying XG concentrations.

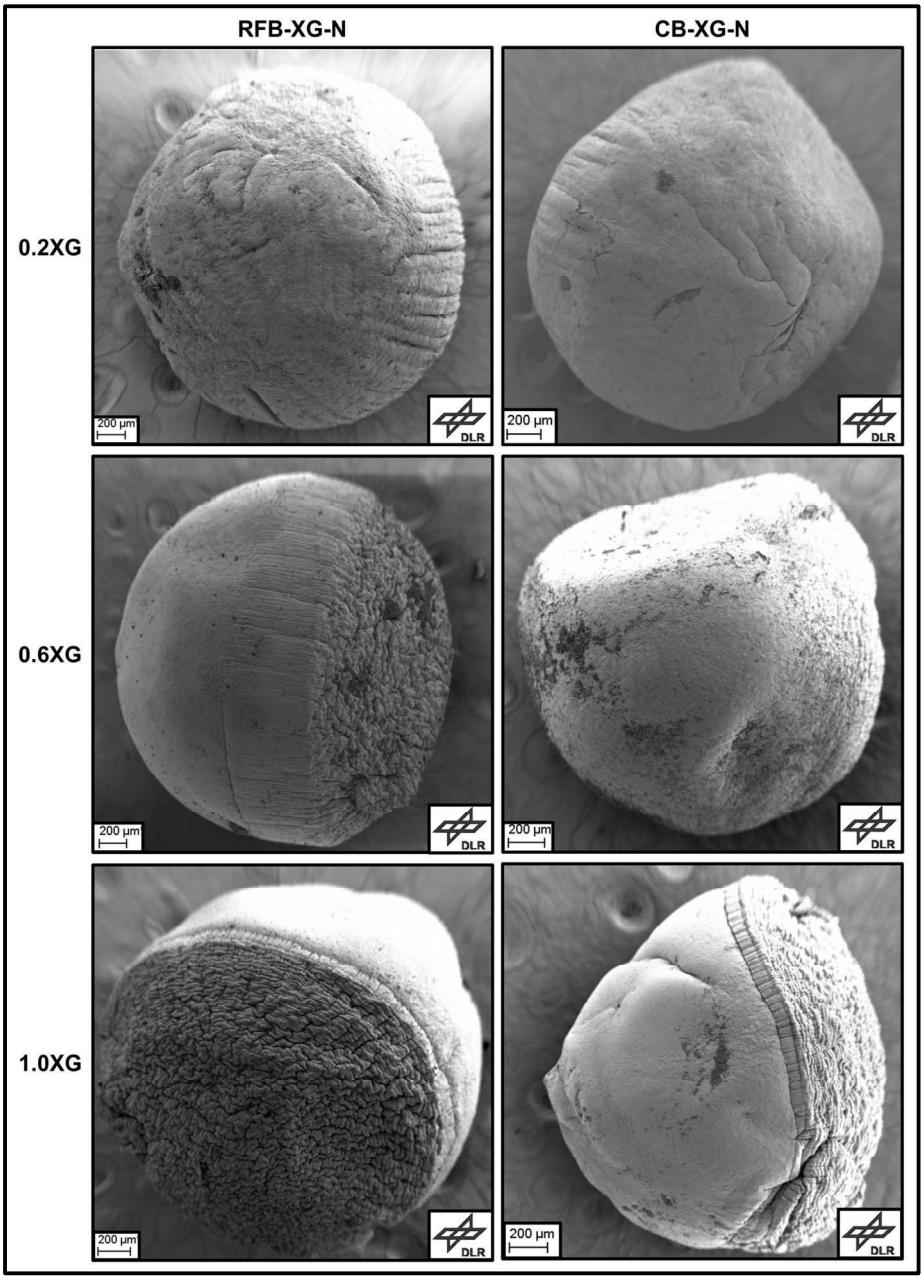

Figure 50: SEM images of RFB-XG-N (left) and CB-XG-N (right) with varying XG concentrations.

The SEM images reveal tear shaped beads with wrinkled surfaces and dents are again observed for both RFB-XG-N and CB-XG-N. In RFB-XG-N with 0.6% and 1.0% XG and CB-1.0XG-N, a very abrupt transition between wrinkled and flat surface can be seen. Since the sol is the same for RFB-XG-H and RFB-XG-N, this appearance might be a result of the higher pH value of the nitric acid gelation bath. Figure 51 shows the internal microstructure of RFB-XG-N and CB-XG-N.

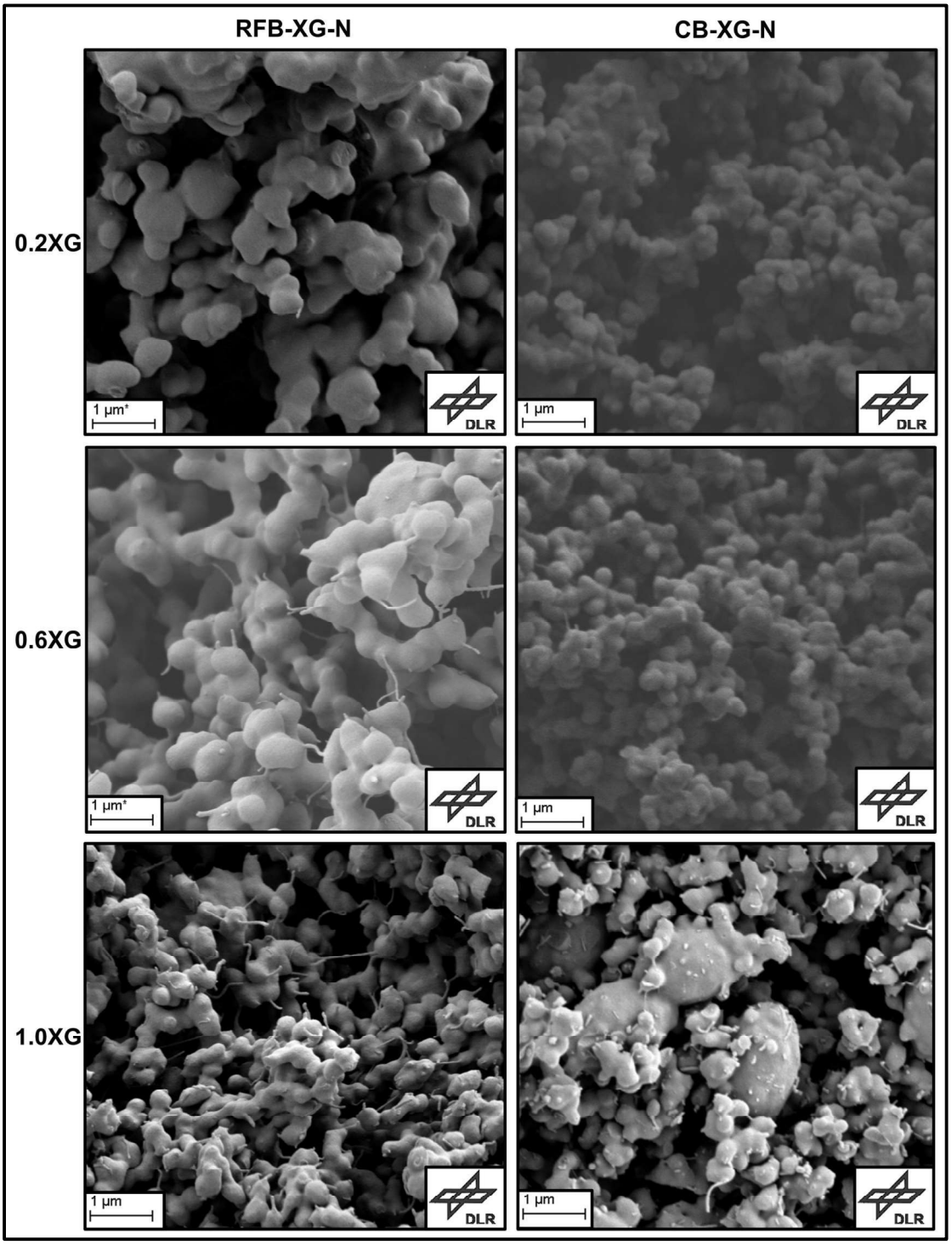

Figure 51: Cross-section SEM images of RFB-XG-N (left) and CB-XG-N (right) with varying XG concentrations.

The microstructure of all shown samples is again composed of nearly spherical particles whose connections look covered, which is in agreement with literature.[3, 15] Particle sizes of few hundred nm and macropores with a size of few microns can be observed. The CB-XG-N samples have smaller particles than RFB-XG-N. Big particles with a size in the micron region can be seen again. Less fibers are observed when these big particles are present. XG fibers might agglomerate at some regions of the sample and lead to these big knots. Figure 52 shows the skeletal- and tapped densities of RFB-XG-N and CB-XG-N with varying XG concentrations.

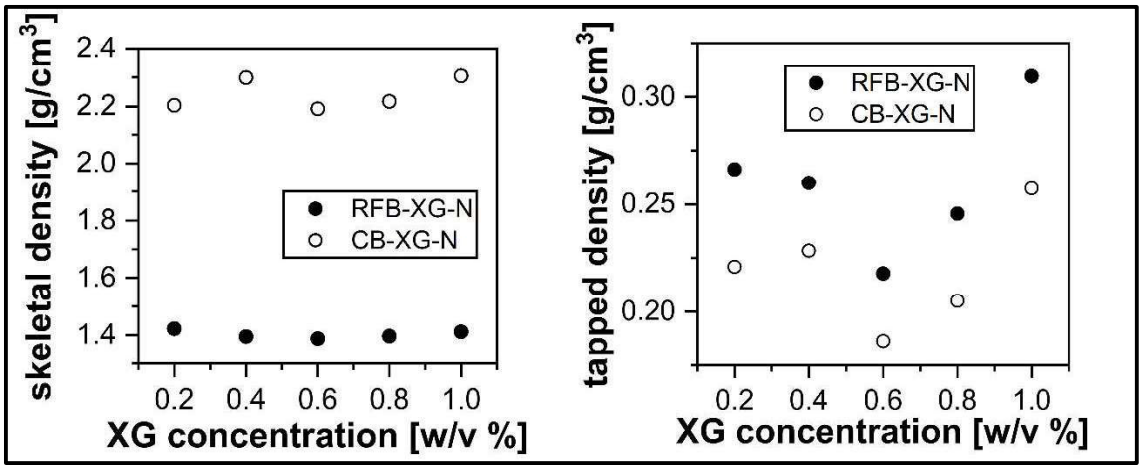

Figure 52: Skeletal- and tapped densities of RFB-XG-N and CB-XG-N with varying XG concentrations.

The skeletal densities of RFB-XG-N are in the region of 1.4 g/cm^3, again a typical value for RF aerogels.[77] CB-XG-N has skeletal densities ranging from 2.2–2.3 g/cm^3 which is again in accordance with values reported in literature.[3] The tapping densities of RFB-XG-N are ranging between 0.22-0.31 g/cm^3 and between 0.19–0.26 g/cm^3 for CB-XG-N. The density values are similar to values for samples dropped in HCl and don't correlate with the XG concentration. Table 10 shows the resulting porosities of RFB-XG-N and CB-XG-N.

Table 10: Porosities of RFB-XG-N and CB-XG-N with varying XG concentrations.

XG conc. [w/v%]	RFB-XG-N Porosity [%]	CB-XG-N Porosity [%]
0.2	81	90
0.4	81	90
0.6	84	92
0.8	82	91
1.0	78	89

The porosities of RFB-XG-N are ranging between 78–84% and the porosities of CB-XG-N are ranging between 89–92%. CB-XG-N samples have a higher porosity than their corresponding RFB-XG-N samples. The porosities are in the same region than for all HCl samples. Figure 53 shows the BET surface area of RFB-XG-N and CB-XG-N with varying XG concentrations.

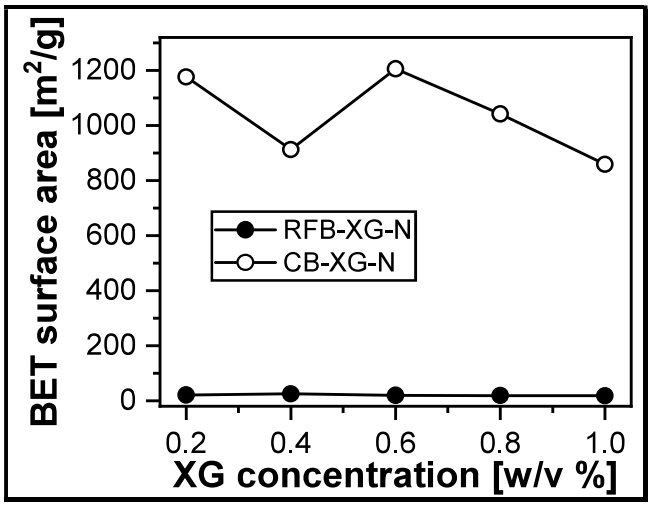

Figure 53: BET surface area of RFB-XG-N and CB-XG-N with varying XG concentration.

The BET surface area of RFB-XG-N is ranging between 18–26 m^2/g, similar to HCl samples. The BET surface area of CB-XG-N is ranging between 856–1206 m^2/g, which is higher than for all HCl samples. Furthermore, there is no correlation with the XG concentration. Table 11 shows the external- and micropore surface area and micropore volumes of CB-XG-N.

Table 11: Additional BET data for CB-XG-N.

Sample	External Surface Area [m^2/g]	Micropore Area [m^2/g]	Micropore Volume [cm^3/g]
CB-XG0.2-N	78	1098	0.42
CB-XG0.4-N	64	849	0.32
CB-XG0.6-N	84	1122	0.43
CB-XG0.8-N	74	968	0.37
CB-XG1.0-N	34	825	0.31

The ratio of external- and micropore surface area reveals a dominating content of micropores in CB-XG-N irrespective of the XG concentration. 825–1122 m^2/g of the surface comes from micropores while only 34–84 m^2/g come from the external surface of the beads. The micropore volume is ranging between 0.31–0.43 cm^3/g and is also

not correlating with the XG-concentration. The micropore volume is higher than for all HCl samples. According to a literature report, boiling activated carbon in HNO_3 resulted in an increase in micropores.[88] Trace amounts of HNO_3 left in the pores of CB might contribute to an increased amount of micropores during carbonization due to a similar effect. Figure 54 shows the DFT calculated pore size distribution of CB-XG-N with varying XG concentrations.

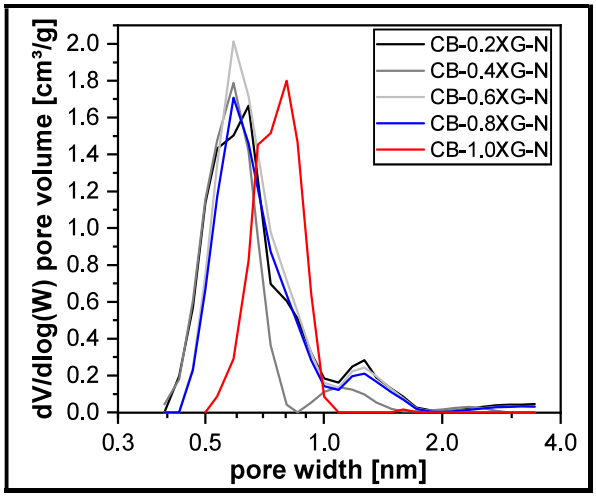

Figure 54: Micropore size distribution of CB-XG-N with varying XG concentrations, calculated by N_2-DFT Model.

All samples show a high amount of micropores with widths ranging between 0.4–1.0 nm and, with exception of CB-1.0XG-N, additional pores with sizes slightly above 1.0 nm. The pore size distributions are similar to the distributions found for HCl samples and the XG concentrations doesn't influence the micropore size distributions of CB-XG-N. Figure 55 shows ATR-IR spectra of RFB-XG-N and CB-XG-N with varying XG concentrations.

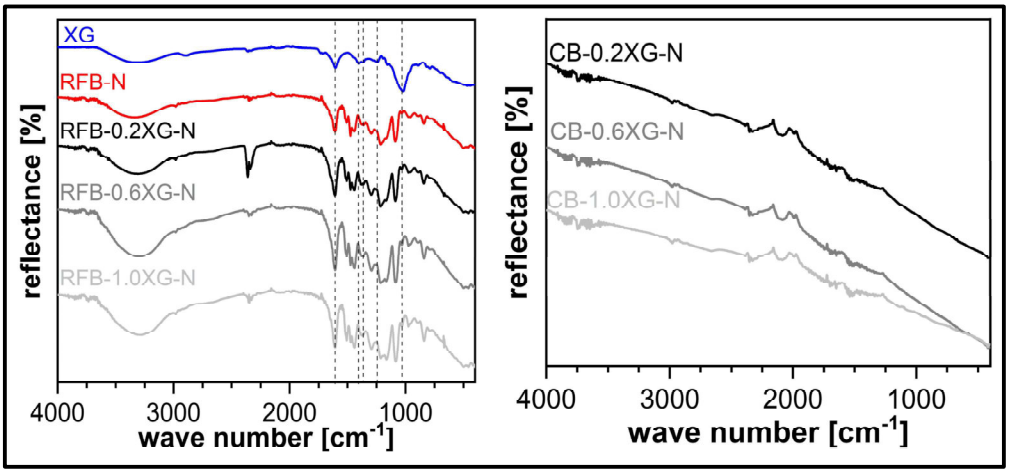

Figure 55: ATR-IR spectra of RFB-XG-N (left) and CB-XG-N (right) with varying XG concentrations. XG reference spectrum is added.

All obtained ATR-IR spectra of RFB-XG-N have the same absorption bands regardless of the XG concentration and are in accordance with literature spectra.[77, 79] The CB-XG-N samples show only a general low reflectance without sharp absorption bands. It is therefore concluded that CB samples don't contain any residual functional groups from RF or XG. Figure 56 shows the WAXS pattern of CB-0.6XG.N.

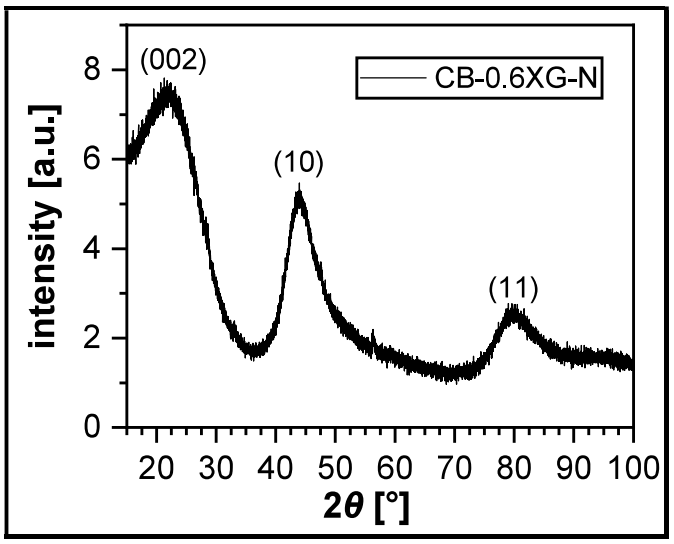

Figure 56: WAXS pattern of CB-0.6XG-N.

The above shown diffractogram shows peaks at 22.0° (002), 43.8° (10) and 80.2° (11) which are in accordance with literature diffractograms of carbon aerogels. The wideness of the peaks is typical for nanocrystalline turbostratic carbons.[3, 87]

To summarize, CB-XG-N samples have higher surface areas and micropore volumes than all CB-XG-H and CBa-XG-H samples. The bead sizes, densities, porosities, surface areas of RFB-XG-N, pore size distributions, IR spectra and XRD diffractograms are similar to HCl samples.

4.6 RF and Carbon Aerogel Beads with Xanthan Gum in HNO_3 – pH adjustment

RFBa-XG-N samples have been produced with XG concentrations varying between 0.2–1.0% and were carbonized afterwards to obtain CBa-XG-N. The pH-value was adjusted to 5.4–5.6 with HNO_3 (0.5M). Figure 57 shows photographs of resulting RFBa-XG-N (left half) and CBa-XG-N (right half) and a table with their respective carbonization yields.

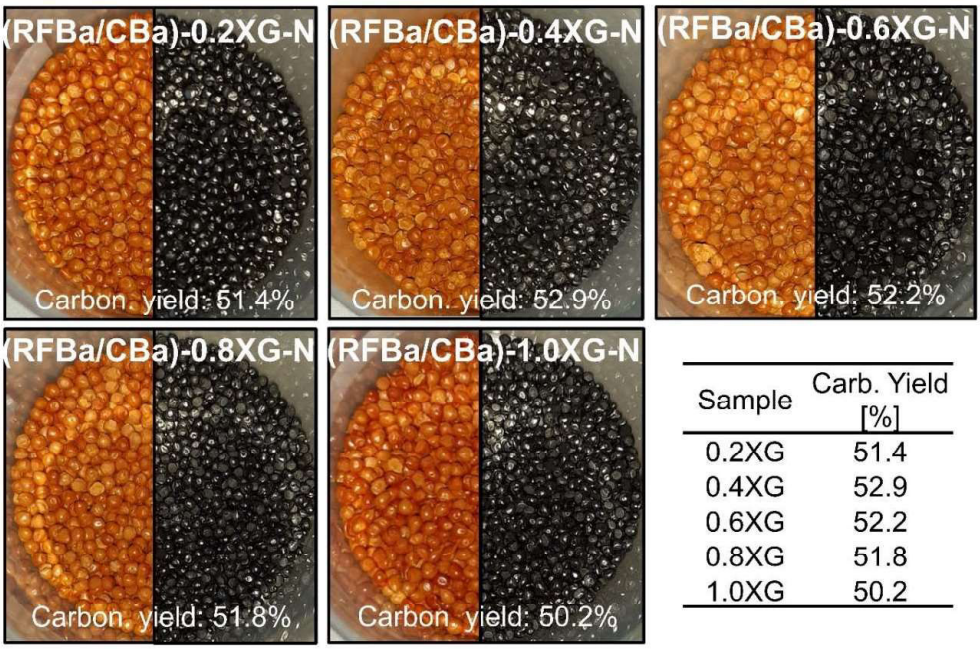

Sample	Carb. Yield [%]
0.2XG	51.4
0.4XG	52.9
0.6XG	52.2
0.8XG	51.8
1.0XG	50.2

Figure 57: Photographs of RFBa-XG-N (left half) and CBa-XG-N (right half) with varying XG concentrations. The carbonization yield is given as mass ratio before and after carbonization.

The resulting RFBa-XG-N samples appear brown/orange and are nearly spherical irrespective of the XG concentration. CBa-XG-N was obtained with carbonization yields ranging between 50.2–52.9% (Fig. 56, table), which are higher than for all previously discussed samples but in accordance with literature.[80] Table 12 gives the average size, standard deviation and vol. shrinkage of selected RFBa-XG-N and CBa-XG-N.

Table 12: Diameter and vol. shrinkage of RFBa-XG-N and CBa-XG-N with varying XG concentrations.

XG conc. [w/v%]	RFBa-XG-N [mm]	CBa-XG-N [mm]	Vol. Shrinkage [%]
0.2	2.41±0.18	2.02±0.16	16.2
0.6	2.46±0.20	2.06±0.17	16.3
1	2.29±0.23	1.91±0.16	16.6

The average RFBa-XG-N size is 2.41 mm (0.2% XG), 2.46 mm (0.6% XG) and 2.29 mm (1.0% XG). There is no direct correlation to the XG concentration, but the standard deviations are rather high, resulting in overlapping size distributions. CBa-XG-N samples generally have smaller sizes than their respective RFBa-XG-N samples. The volumetric shrinkage after carbonization is ranging between 16.2–16.6%, which is slightly lower than literature values.[81]The bead sizes are similar to all other samples. Figure 58 shows overview SEM images of RFBa-XG-N and CBa-XG-N with varying XG concentrations.

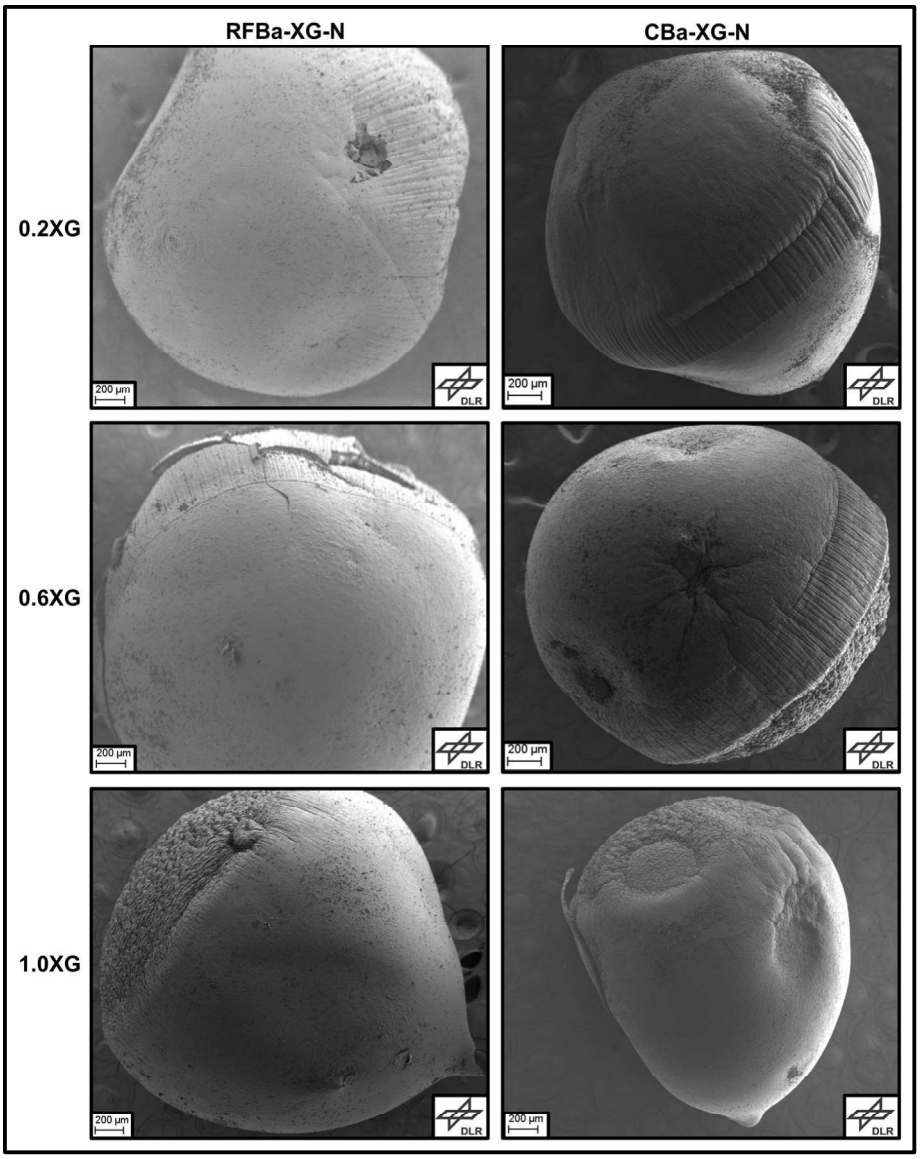

Figure 58: SEM images of RFBa-XG-N (left) and CBa-XG-N (right) with varying XG concentrations.

The SEM images reveal tear shaped beads with wrinkled surfaces and dents are again observed for both RFBa-XG-N and CBa-XG-N. Similar as in RFB-XG-N and CB-XG-N again abrupt transition between flat and wrinkled surface is exhibited for

CBa-0.6XG-N, RFBa-1.0XG-N and CBa-1.0XG-N. Figure 59 shows the internal microstructure of RFBa-XG-N and CBa-XG-N.

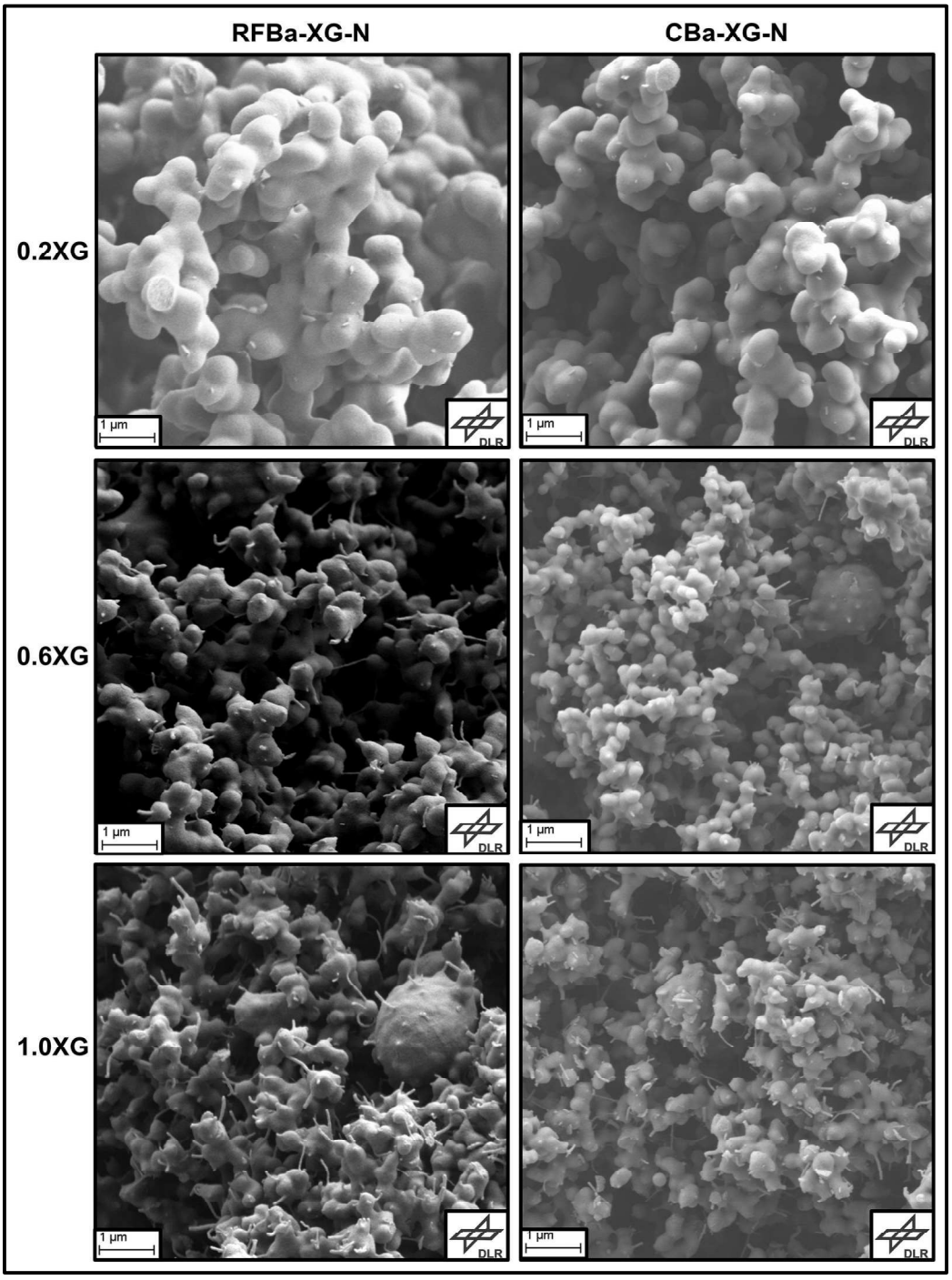

Figure 59: Cross-section SEM images of RFBa-XG-N (left) and CBa-XG-N (right) with varying XG concentrations.

The microstructure of all shown samples is again composed of nearly spherical particles whose connections look covered, which is in agreement with literature.[3, 15] Particle sizes of few hundred nm and macropores with a size of few microns can be observed. The CBa-XG-N samples generally have a smaller particle size than their

RFBa-XG-N precursors. Micron sized particles and less fibers can be seen again, indicating agglomeration of XG. Figure 60 shows the skeletal densities and tapped densities of RFBa-XG-N and CBa-XG-N with varying XG concentrations.

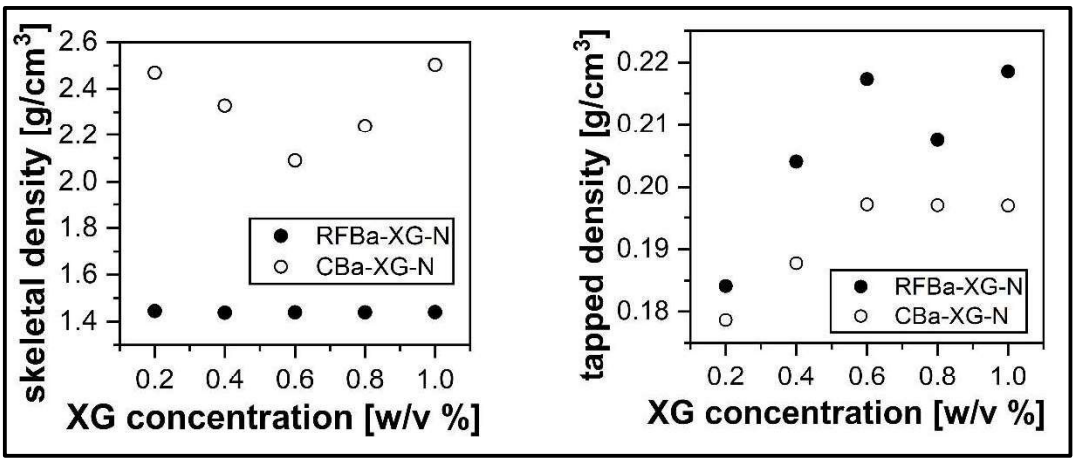

Figure 60: Skeletal- and tapped densities of RFBa-XG-N and CBa-XG-N with varying XG concentrations.

The skeletal densities of RFBa-XG-N are in the region of 1.4 g/cm^3, which are typical values for RF aerogels.[77] CBa-XG-N has skeletal densities ranging from 2.1–2.5 g/cm^3 which is again in accordance with values reported in literature.[3] The tapped densities of RFBa-XG-N are ranging between 0.20–0.22 g/cm^3 and 0.18–0.20 g/cm^3 for CBa-XG-N. The tapped density values are slightly lower compared to all other samples. Table 13 shows the resulting porosities of RFBa-XG-N and CBa-XG-N.

Table 13: Porosities of RFBa-XG-N and CBa-XG-N with varying XG concentrations.

XG conc. [w/v%]	RFBa-XG-N Porosity [%]	CBa-XG-N Porosity [%]
0.2	87	93
0.4	86	92
0.6	85	91
0.8	86	91
1.0	85	92

The porosities of RFBa-XG-N are ranging between 85–87% and 91–93% for CBa-XG-N. The values are comparable with the values for alle other samples discussed in this thesis. CBa-XG-N samples have a higher porosity than their corresponding RFBa-XG-N precursors. Figure 61 shows the BET surface area of RFBa-XG-N and CBa-XG-N with varying XG concentrations.

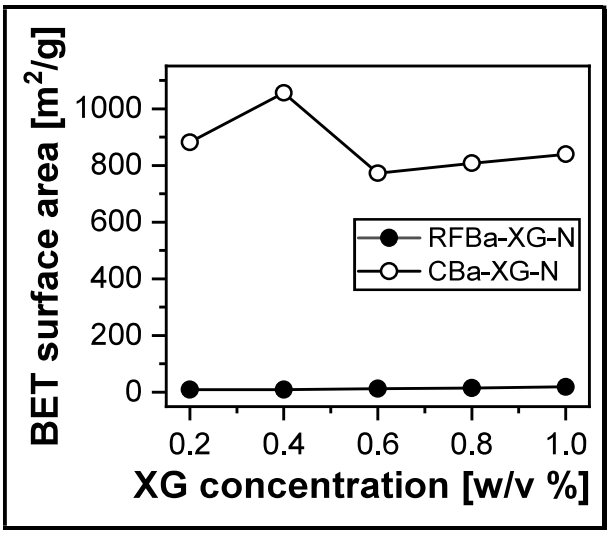

Figure 61: BET surface area of RFBa-XG-N and CBa-XG-N with varying XG concentrations.

The BET surface area of RFBa-XG-N is ranging between 10–19 m^2/g, increasing with XG concentration and lower than for RFB-XG-N. The BET surface area of CBa-XG-N is ranging between 772–1056 m^2/g, not correlating with the XG concentration and lower than for CB-XG-N. Table 14 shows the external- and micropore surface area and micropore volumes of CBa-XG-N.

Table 14: Additional BET data for CBa-XG-N with varying XG concentrations.

Sample	External Surface Area [m^2/g]	Micropore Area [m^2/g]	Micropore Volume [cm^3/g]
CBa-XG0.2-N	54	828	0.32
CBa-XG0.4-N	75	981	0.37
CBa-XG0.6-N	61	711	0.27
CBa-XG0.8-N	61	747	0.29
CBa-XG1.0-N	53	786	0.30

The ratio of external- and micropore surface area reveals a dominating content of micropores in CBa-XG-N irrespective of the XG concentration. 711–981 m^2/g of the surface comes from micropores while only 53–75 m^2/g come from the external surface of the beads. The micropore volume is ranging from 0.27–0.37 cm^3/g and is also lower than for CB-XG-N and not correlating with the XG-concentration. Figure 62 shows the DFT calculated pore size distribution of CBa-XG-N with varying XG concentrations.

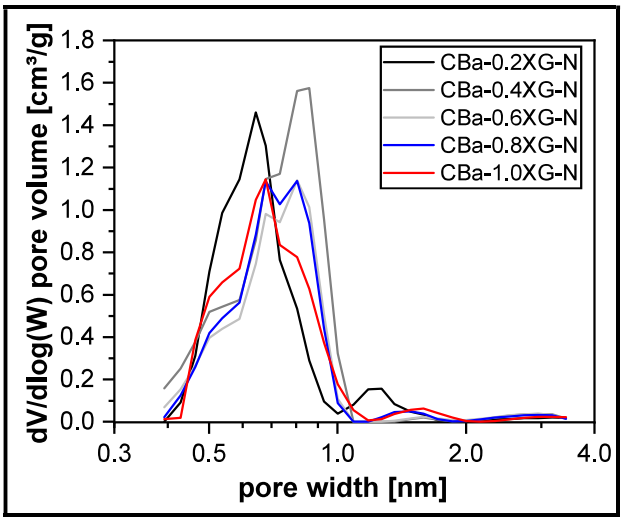

Figure 62: Micropore size distribution of CBa-XG-N with varying XG concentrations, calculated by N_2-DFT Model.

All samples show a high amount of micropores with widths ranging between 0.4–1.0 nm and additional pores with sizes slightly above 1.0 nm. The XG concentrations doesn't influence the micropore size distributions of CBa-XG-N and the size distributions are comparable to all other samples. Figure 63 shows ATR-IR spectra of RFBa-XG-N and CBa-XG-N with varying XG concentrations.

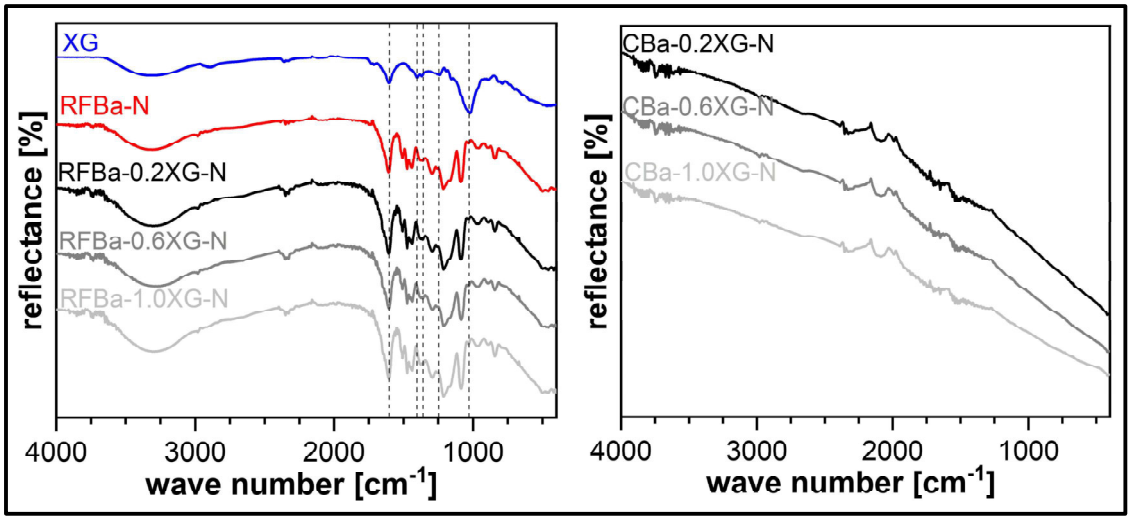

Figure 63: ATR-IR spectra of RFBa-XG-N (left) and CBa-XG-N (right) with varying XG concentrations. XG reference spectrum is added.

All obtained ATR-IR spectra of RFB-XG-N have the same absorption bands regardless of the XG concentration and are in accordance with literature spectra.[77, 79] The CBa-XG-N samples show only a general low reflectance without sharp absorption bands. It is therefore concluded that CB samples don't contain any residual functional groups from RF or XG. Figure 64 shows the WAXS pattern of CBa-0.6XG-N.

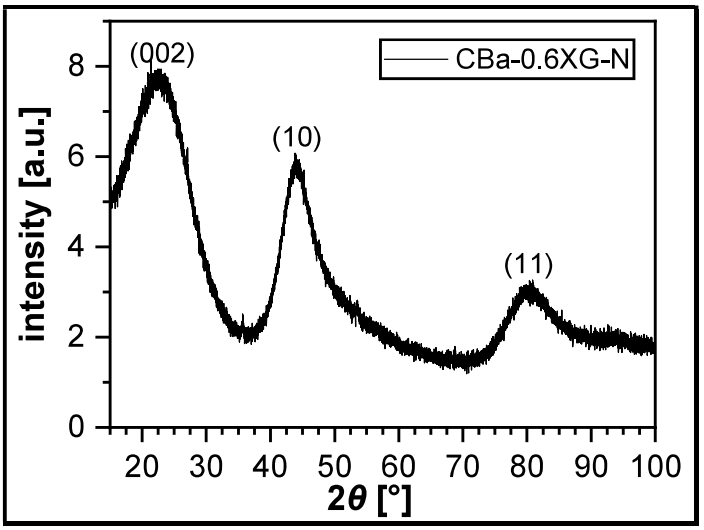

Figure 64: WAXS pattern of CBa-0.6XG-N.

The above shown diffractogram shows peaks at 22.7° (002), 44.0° (10) and 80.5° (11) which are in accordance with literature diffractograms of carbon aerogels. The wideness of the peaks is typical for nanocrystalline turbostratic carbons.[3, 87]

To summarize, CBa-XG-N samples have lower densities, surface areas and micropore volumes than CB-XG-N. The bead sizes, porosities, pore size distributions, IR spectra and XRD diffractograms are similar to RFB-XG-N and CB-XG-N.

5. Summary

A dropping process for the preparation of RF aerogel microbeads has successfully been developed. XG containing RF sol was pre-gelled under basic conditions and dropped into an acidic gelation bath afterwards. The samples were successfully carbonized to obtain carbon aerogel microbeads. The influence of the XG concentration, HCl and HNO_3 as gelation baths and pH adjustment of the sol have been investigated. The resulting beads were characterized in terms of appearance, average bead size, microstructure, skeletal- and tapped densities, porosities, BET surface areas, micropore surface areas and volumes, ATR-IR spectroscopy and WAXS.

Samples w/o XG addition had an irregular flake shape but otherwise typical microstructures, skeletal densities (1.42–1.48 g/cm^3), BET surface areas (13–75 m^2/g) and ATR-IR spectra for RF aerogels.

XG containing RFB samples appeared brown/orange while CB samples appeared black with nearly spherical shapes, irrespective of XG concentration, pH adjustment and gelation bath. Average bead sizes of all RFB samples were ranging

between 2.18–2.56 mm and increasing with XG concentration in the case of RFB-XG-H and RFBa-XG-H. CB samples always had smaller average sizes (1.75–2.06 mm) than their respective RFB precursors. The volumetric shrinkage upon carbonization was ranging between 21.1–25.0% for RFB-XG-H, RFBa-XG-H and RFB-XG-N and between 16.2-16.6% for RFBa-XG-N. The carbonization yields were ranging between 40–50%.

SEM images revealed tear- and oblate shaped beads with wrinkled surfaces that had some dents irrespective of XG concentration, pH adjustment and gelation bath. A typical microstructure for base-acid catalyzed RF aerogels was observed in each RFB sample. Nearly spherical covered particles with sizes in the region of few hundred nm and macropore sizes in the region of few microns were observed. CB samples typically had smaller particles than their respective RFB precursors. With increasing XG concentration more fibers were visible in the microstructure. RF particles grow on top of the fibers and are interconnected by the fibers. In some cases, big micron sized particles and less fibers were observed at the same time even for high XG concentrations.

The skeletal- and tapped densities of all RFB samples were ranging between 1.39–1.44 g/cm^3 and 0.17–0.32 g/cm^3 irrespective of the XG concentration, pH adjustment and gelation bath. The skeletal- and tapped densities of all CB samples were ranging between 2.1–2.5 g/cm^3 and 0.18–0.31 g/cm^3 irrespective of the XG concentration, pH adjustment and gelation bath. The porosities were ranging between 78–88% for RF samples and 86–93% for CB samples irrespective of the XG concentration, pH adjustment and gelation bath.

The BET surface areas of RFB-XG-H were ranging between 15–37 m^2/g. RFBa-XG-H samples had a slightly lower BET surface area ranging between 9–19 m^2/g. RFB-XG-N and RFBa-XG-N had BET surface areas of 18–26 m^2/g and 10–19 m^2/g respectively. CB samples had significantly higher surfaces areas compared to RF. CB-XG-H exhibited BET surface areas ranging between 785–978 m^2/g while CBa-XG-H exhibited BET surface areas ranging between 687–860 m^2/g. HNO_3 samples exhibited BET surface areas of 856–1206 m^2/g (CB-XG-N) and 772–1056 m^2/g (CBa-XG-N). The XG concentration had no influence on the BET surface areas, pH adjustment resulted in lower surface areas and using HNO_3 as gelation bath resulted in higher surface areas in case of CB samples.

A similar trend was observed for the micropore volume of CB samples. The

micropore volume of CB-XG-H was ranging between 0.28–0.35 cm^3/g and 0.25–0.31 cm^3/g for CBa-XG-H. For HNO_3 samples the values were ranging between 0.31–0.43 cm^3/g (CB-XG-N) and 0.27–0.37 cm^3/g (CBa-XG-N). The micropore size distribution was with peaks between 0.4–1.0 nm similar for each sample irrespective of XG concentration, pH adjustment and gelation bath.

The ATR-IR spectra exhibited typical absorption bands of RF aerogels and was similar for each sample irrespective of XG concentration, pH adjustment and gelation bath. CB samples showed an overall lower reflectance without adsorption bands.

WAXS patterns showed the typical peaks for carbon aerogels and were similar for each sample irrespective of XG concentration, pH adjustment and gelation bath.

6. Future Direction

In future experiments, the beads can be further analyzed concerning their mechanical properties, thermal conductivities, and gas permeabilities. Even though the addition of XG has not significantly altered the properties of the beads discussed in this thesis, other properties might be influenced. Based on these results an optimal XG concentration can be chosen to fit the properties for foundry applications.

Furthermore, the interaction between XG and RF can be studied with NMR spectroscopy. The gelation mechanism of RF catalyzed by HCl has been studied in a similar way previously.[77]

Moreover the leached out material should be characterized and prevention of the leaching should be investigated. Approaches like using surfactants in the gelation bath or an ethanolic HCl solution as gelation bath could be considered.

The upscaling of the bead production might be realized by application of the JetCutter technology. Major challenges are safety issues due to formaldehyde usage and finding the right parameters of the JetCutter and the right viscosity of the sol. Therefore, the viscosity of RF sols with varying XG concentrations should be investigated with a rheometer or with a viscosimeter.

The beads can also be used for other applications like catalysis. Coating the beads with a catalytic active metal or functionalization of the beads might lead to catalytic active RF aerogel beads. Alternatively, novel functionalized precursors can be used during the RF synthesis itself.

7. References

[1] a) K. Ganesan, T. Budtova, L. Ratke, P. Gurikov, V. Baudron, I. Preibisch, P. Niemeyer, I. Smirnova, B. Milow, *Materials* **2018**, *11*, 2144;
b) L. Druel, P. Niemeyer, B. Milow, T. Budtova, *Green Chem.* **2018**, *20*, 3993-4002.

[2] a) C. T. Alviso, R. W. Pekala, J. Gross, X. Lu, R. Caps, J. Fricke, *Mater. Res. Soc. Symp. Proc.* **1996**, *431*, 521;
b) S. T. Mayer, F. M. Kong, R. W. Pekala, J. L. Kaschmitter*, U.S. Pat. 5 908 896*, United States of America, **1999**;
c) T. Horikawa, J. i. Hayashi, K. Muroyama, *Carbon* **2004**, *42*, 169-175;
d) N. Liu, S. Zhang, R. Fu, M. S. Dresselhaus, G. Dresselhaus, *Carbon* **2006**, *44*, 2430-2436;
e) J. Chaichanawong, K. Kongcharoen, S. Areerat, *Adv. Powder Technol.* **2013**, *24*, 891-896;
f) V. Baudron, P. Gurikov, I. Smirnova, *Colloid. Surface A* **2019**, *566*, 58-69.

[3] M. Schwan, J. Schettler, F. M. Badaczewski, C. Heinrich, B. M. Smarsly, B. Milow, *J. Mater. Sci.* **2020**, *55*, 5861-5879.

[4] I. Preibisch, P. Niemeyer, Y. Yusufoglu, P. Gurikov, B. Milow, I. Smirnova, *Materials* **2018**, *11*, 1287.

[5] a) M. Schwan, *Dissertation* **2018**, *Rheinisch-Westfälische Technische Hochschule Aachen*;
b) D. Naaß, *Unpublished Results, DLR* **2019**.

[6] I. Preibisch, P. Niemeyer, Y. Yusufoglu, P. Guirkov, B. Milow, I. Smirnova, *Materials* **2018**, *11*, 1287.

[7] a) J. Milani, G. Maleki, in *Hydrocolloids in Food Industry*, **2012**;
b) D. Saha, S. Bhattacharya, *J. Food Sci. Technol.* **2010**, *47*, 587-597.

[8] a) L. Ratke, B. Milow, in *Aerogel Handbook*, **2011**, 763-788;
b) L. Ratke, S. Brück*, Euro. Pat. 1 820 582 A1*, Germany, **2007**.

[9] www.steeldata.info, **08.02.2021**.

[10] www.giessereilexikon.com, **08.02.2021**.

[11] L. Ratke, *Aerogels - A Practical Workshop*, **2018**.

[12] A. M. El-Khatat, S. A. Al-Muhtaseb, *Adv. Mater.* **2011**, *23*, 2887-2903.

[13] M. Schwan, M. Naikade, D. Raabe, L. Ratke, *J. Mater. Sci.* **2015**, *50*, 5482-5493.

[14] B. Milow, S. Ludwig, L. Ratke, *Citric Acid Catalyzed Gelation of RF-Aerogels*, Conference Paper, **2011**.

[15] J. Laskowski, B. Milow, L. Ratke, *Micropor. Mesopor. Mat.* **2014**, *197*, 308-315.

[16] a) N. Job, A. Théry, R. Pirard, J. Marien, L. Kocon, J.-N. Rouzaud, F. Béguin, J.-P. Pirard, *Carbon* **2005**, *43*, 2481-2494;
b) R. Saliger, U. Fischer, C. Herta, J. Fricke, *J. Non-Cryst. Solid.* **1998**, *225*, 81-85.

[17] N. Tonanon, Y. Wareenin, A. Siyasukh, W. Tanthapanichakoon, H. Nishihara, S. R. Mukai, H. Tamon, *J. Non-Cryst. Solids* **2006**, *352*, 5683-5686.

[18] R. W. Pekala, C. T. Alviso, X. Lu, J. Gross, J. Fricke, *J. Non-Cryst. Solids* **1995**, *188*, 34-40.

[19] G. Biesmans, A. Mertens, L. Duffours, T. Woignier, J. Phalippou, *J. Non-Cryst. Solids* **1998**, *225*, 64-68.

[20] J. Yamashita, T. Ojima, M. Shioya, H. Hatori, Y. Yamada, *Carbon* **2003**, *41*, 285-294.

[21] V. Budarin, J. H. Clark, J. E. Hardy, R. Luque, K. Milkowski, S. J. Tavener, A. J. Wilson, *Angew. Chem. Int. Ed.* **2006**, *45*, 3782-3786.

[22] R. J. White, V. L. Budarin, J. H. Clark, *Chem. Eur. J.* **2010**, *16*, 1326-1335.

[23] R. J. White, C. Antonio, V. L. Budarin, E. Bergström, J. Thomas-Oates, J. H. Clark, *Adv. Funct. Mater.* **2010**, *20*, 1834-1841.

[24] B. Milow, L. Ratke, *Gießerei-Rundschau* **2012**, *59*, 74-81.

[25] S. S.-L. Mulik, Chariklia, in *Aerogels Handbook*, Springer, New York, **2011**, 215-234.

[26] L. Zuo, Y. Zhang, L. Zhang, Y.-E. Miao, W. Fan, T. Liu, *Materials* **2015**, *8*, 6806-6848.

[27] a) G. Rasines, P. Lavela, C. Macías, M. C. Zafra, J. L. Tirado, J. B. Parra, C. O. Ania, *Carbon* **2015**, *83*, 262-274;
b) M. Seredych, K. László, T. J. Bandosz, *ChemCatChem* **2015**, *7*, 2924-2931.

[28] C. Moreno-Castilla, F. J. Maldonado-Hódar, *Carbon* **2005**, *43*, 455-465.

[29] J. Shen, D. Y. Guan, in *Aerogels Handbook*, Springer New York, New York, **2011**, 813-831.

[30] F. Li, L. Xie, G. Sun, F. Su, Q. Kong, Q. Li, Y. Chao, X. Guo, C. Chen, *ChemElectroChem* **2017**, *4*, 3119-3125.

[31] en.wikipedia.org/wiki/Sand_casting, **08.02.2021**.

[32] M. Bakierska, A. Chojnacka, M. Świętosławski, P. Natkański, M. Gajewska, M. Rutkowska, M. Molenda, *Materials* **2017**, *10*, 1336.

[33] M. Alnaief, I. Smirnova, *J. Supercrit. Fluids* **2011**, *55*, 1118-1123.

[34] P. Paraskevopoulou, D. Chriti, G. Raptopoulos, G. C. Anyfantis, *Materials* **2019**, *12*, 1543.

[35] S. Gu, C. Zhai, S. C. Jana, *Langmuir* **2016**, *32*, 5637-5645.

[36] M. Alnaief, M. A. Alzaitoun, C. A. García-González, I. Smirnova, *Carbohydr. Polym.* **2011**, *84*, 1011-1018.

[37] M. Alnaief, R. Obaidat, H. Mashaqbeh, *Carbohydr. Polym.* **2018**, *180*, 264-275.

[38] C. A. García-González, E. Carenza, M. Zeng, I. Smirnova, A. Roig, *RSC Adv.* **2012**, *2*, 9816-9823.

[39] U. Prüße, U. Jahnz, P. Wittlich, J. Breford, K.-D. Vorlop, *Landbauforsch. Völkenrode* **2002**, *241*, 1-10.

[40] D. Chriti, G. Raptopolous, M. Papastergiou, P. Paraskevopoulou, *Gels* **2018**, *4*, 66.

[41] M. Robitzer, F. D. Renzo, F. Quignard, *Micropor. Mesopor. Mat.* **2011**, *140*, 9-16.

[42] S. M. Kamal Mohamed, K. Ganesan, B. Milow, L. Ratke, *RSC Adv.* **2015**, *5*, 90193-90201.

[43] A. Veronovski, G. Tkalec, Ž. Knez, Z. Novak, *Carbohydr. Polym.* **2014**, *113*, 272-278.

[44] J. A. Kenar, F. J. Eller, F. C. Felker, M. A. Jackson, G. F. Fanta, *Green Chem.* **2014**, *16*, 1921-1930.

[45] www.nanohybrids.eu, **08.02.2021**.

[46] J. Laskowski, Rheinisch-Westfälische Technische Hochschule Aachen **2016**.

[47] J. Goodwin, R. Hughes, *Rheology for Chemists*, RSC Publishing, **2008**.

[48] Halliday, Resnick, Walker, *Halliday Physik - Bachelor Edition*, Wiley-VCH, **2013**.

[49] B. Hochstein, R. Brummer, *Rheologische Grundlagen und Relevanz in der kosmetischen Industrie*, Behr, Hamburg, **2012**.

[50] https://de.wikipedia.org/wiki/Viskosit%C3%A4t, **08.02.2021**.

[51] *Practigal Guide to Rheology Modifiers*, BASF SE, Ludwigshafen.

[52] M. Karsheva, S. Georgieva, S. Handijeva, *J. Univ. Chem. Technol. Metallurgy* **2007**, *42*, 187-194.

[53] a) J. Shokri, K. Adibkia, in *Cellulose - Medical, Pharmaceutical and Electronic Applications*, IntechOpen, **2013**;
b) J. Grove, M. Durr, M.-P. Quint, B. Plazonnet, *Int. J. Pharm.* **1990**, *66*, 23-28.

[54] D. Thorburn Burns, R. J. Lewis, J. Bridges, *Anal. Chim. Acta* **1998**, *375*, 255-260.

[55] K. C. Taylor, H. A. Nasr-El-Din, *J. Petrol. Sci. Eng.* **1998**, *19*, 265-280.

[56] a) K.-W. Song, Y.-S. Kim, G.-S. Chang, *Fibers Polym.* **2006**, *7*, 129-138;
b) http://www.colltec.de/Xanthan_Gum/xanthan_gum.html, **08.02.2021**;
c) https://de.wikipedia.org/wiki/Xanthan, **08.02.2021**.

[57] S. Sethi, Saruchi, B. S. Kaith, M. Kaur, N. Sharma, V. Kumar, *Cellulose* **2020**, *27*, 4565-4589.

[58] http://www.colltec.de/Xanthan_Gum/xanthan_gum.html, **08.02.2021**.

[59] R. A. Speers, M. A. Tung, *J. Food Sci.* **1986**, *51*, 96-98.

[60] P. J. Whitcomb, C. W. Macosko, *J. Rheol.* **1978**, *22*, 493-505.

[61] Deuteron, *Thickening Agents - Biopolymers for viscosity control of aqueous systems*, Handout, **2020**.

[62] A. H. Dhiaa, *Kufa J. Eng.* **2012**, *3*, 17-30.

[63] L. Xu, G. Y. Xu, L. Yu, H. J. Gong, M. Z. Dong, Y. J. Li, *Polym. Advan. Technol.* **2014**, *25*, 1122-1129.

[64] Y. Wu, W. Ding, L. Jia, Q. He, *Food Chem.* **2015**, *168*, 366-371.

[65] J. L. Doublier, B. Launay, *J. Texture Stud.* **1981**, *12*, 151-172.

[66] W. Sittikijyothin, D. Torres, M. P. Gonçalves, *Carbohydr. Polym.* **2005**, *59*, 339-350.

[67] J. A. Casas, A. F. Mohedano, F. García-Ochoa, *J. Sci. Food Agric.* **2000**, *80*, 1722-1727.

[68] K. N. Venugopal, M. Abhilash, *Int. J. Pharm. Sci. Res.* **2010**, *1*, 28-39.

[69] H. El Batal, A. Hasib, A. Ouatmane, A. Jaouad, M. Naïmi, *Rev. Gen. Ind.* **2012**, *8*, 55-62.

[70] E. Onsøyen, in *Thickening and Gelling Agents for Food* (Ed.: A. P. Imeson), Springer US, Boston, MA, **1997**, 22-44.

[71] D. J. McHugh, *FAO Fish. Tech. Pap.* **1987**, *288*, 58-115.

[72] S. M. Kamal Mohamed, *Unpublished Results, DLR* **2019**.

[73] T. Anklam, *Unpublished Results, DLR* **2020**.

[74] M. Thommes, K. Kaneko, A. V. Neimark, J. P. Olivier, F. Rodriguez-Reinoso, J. Rouquerol, K. S. W. Sing, *Pure Appl. Chem.* **2015**, *87*, 1051-1069.

[75] A. Léonard, S. Blacher, M. Crine, W. Jomaa, *J. Non-Cryst. Solids* **2008**, *354*, 831-838.

[76] E. S. Chan, B. B. Lee, P. Ravindra, D. Poncelet, *J. Colloid Interface Sci.* **2009**, *338*, 63-72.

[77] S. Mulik, C. Sotiriou-Leventis, N. Leventis, *Chem. Mater.* **2007**, *19*, 6138-6144.

[78] W. D. King, F. F. Fondeur, W. R. Wilmarth, M. E. Pettis, S. W. McCollum, *Sep. Sci. Technol.* **2006**, *41*, 2475-2486.

[79] R. W. Pekala, *J. Mater. Sci.* **1989**, *24*, 3221-3227.

[80] C. Lin, J. A. Ritter, *Carbon* **2000**, *38*, 849-861.

[81] R. Saliger, V. Bock, R. Petricevic, T. Tillotson, S. Geis, J. Fricke, *J. Non-Cryst. Solids* **1997**, *221*, 144-150.

[82] a) R. Petričević, M. Glora, A. Möginger, J. Fricke, *J. Non-Cryst. Solids* **2001**, *285*, 272-276;
b) Y. Zhong, B. Zhou, J. Gui, A. Du, Z. Zhang, J. Shen, *Fusion Eng. Des.* **2011**, *86*, 238-243.

[83] T. Kobori, A. Matsumoto, S. Sugiyama, *Carbohydr. Polym.* **2009**, *75*, 719-723.

[84] J. Shen, J. Hou, Y. Guo, H. Xue, G. Wu, B. Zhou, *J. Sol-Gel Sci. Technol.* **2005**, *36*, 131-136.

[85] V. Bock, A. Emmerling, J. Fricke, *J. Non-Cryst. Solids* **1998**, *225*, 69-73.

[86] S. Faria, C. de Oliveira Petkowicz, S. de Morais, M. Terrones, M. de Resende, F. de França, V. Cardoso, *Carbohydr. Polym.* **2011**, *86*, 469-476.

[87] a) M. Yan, L. Zhang, R. He, Z. Liu, *J. Porous Mater.* **2015**, *22*, 699-703;
b) J. Li, X. Wang, Q. Huang, S. Gamboa, P. J. Sebastian, *J. Power Sources* **2006**, *158*, 784-788;
c) S. Singh, A. Bhatnagar, V. Dixit, V. Shukla, M. A. Shaz, A. S. K. Sinha, O. N. Srivastava, V. Sekkar, *Int. J. Hydrog. Energy* **2016**, *41*, 3561-3570;
d) C. Lin, J. A. Ritter, *Carbon* **1997**, *35*, 1271-1278.

[88] P. Su, J. Zhang, J. Tang, C. Zhang, *Water Sci. Technol.* **2019**, *80*, 86-97.